Studying reaction kinetics using x-ray probes

Master's Thesis
by
Henrik Segerbäck

Lund Reports on Atomic Physics, LRAP-320
Lund May 2004

Abstract

This thesis describes an initial investigation of the experimental requirements for studying the temporal development of a laser-initiated chemical reaction using storage-ring generated x-ray probe pulses.

The beamline D611 with its attached laser setup at the Maxlab synchrotron radiation facility is a possible experimental environment and has been used as an example in calculations.

Several different complexes with associated photo-induced reactions that would be interesting to study are investigated from a time-resolved experiment feasability viewpoint.

Photon flux at D611 turned out to be too low at most energies for picosecond-resolution experiments, and very difficult at best at optimal energies (slightly below 6 keV). Events a few nanoseconds in duration, however, appear to be possible to study over a large energy region, stretching towards high energies (around 10 keV).

Working at 10 keV instead of around 3 keV would simplify the experiments a great deal. Absorption in essentially all solvents considered ceases to be a problem, the experiment can be carried out in air instead of vacuum or helium, and the walls of experimental cells can be made of commonly used materials.

Contents

1 Introduction

General discussion about x-ray absorption techninques, such as that presented in this and the next chapter, is available in [1, 2, 3, 4].

A common way of studying the kinetics of a chemical reaction involves initiating the reaction with a laser pulse and then passing a laser pulse through the sample in order to probe the reaction state. To study development over time, this procedure is repeated with different delays between the two laser pulses. The wavelength of the probe pulse is chosen to match a wavelength region in which the absorption of the sample molecules closely relates to the property to be studied.

Unfortunately, for some reactions there is no appropriate absorption to monitor in the wavelength region available from laser systems. For those, one option would be to study changes in x-ray absorption (see Figure 1 below) at a particularly interesting energy, namely a "band edge" (see Chapter 2 for details). This yields information about the oxidation state of the atom studied, and not rarely about other properties such as the chemical environment as well.

For any element, there are typically several band edges that can be monitored. Since each band edge spans a very narrow region of the x-ray energy space, it is very likely that each element included in a complex will have a distinct band edge that can be studied.

In organometallic complexes with a single metal centre surrounded by organic ligands[1], important information about the chemistry of the complex can be obtained by watching the state of the metal centre. The oxidation state of exactly that one atom can be studied by probing one of its band edges. Similarly, in organometallic complexes with several different-element metal centres, the oxidation state of each of these centres can be independently monitored.

This thesis presents an investigation into experiments such as those outlined above, the ultimate objective being to study the short-timescale reactions that take place in complexes intended for use in solar cells based on artificial photosynthesis.

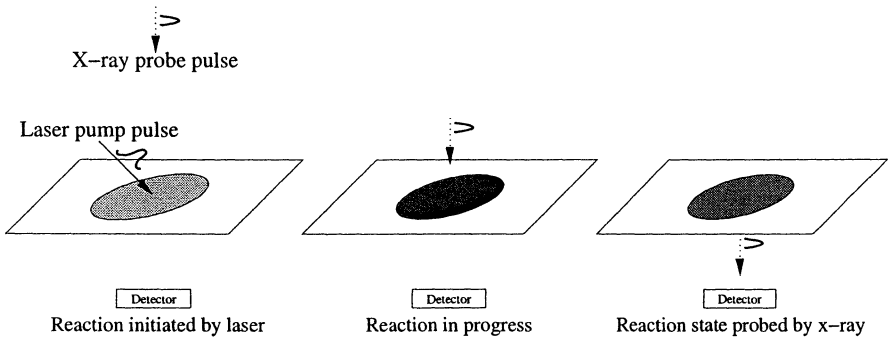

Figure 1: Method proposed for following reaction-time development. The reaction is initiated by a short laser pulse hitting the sample. After an adjustable delay, a monochromatic x-ray pulse passes through the same part of the sample. By analysing the intensity of the output x-ray pulse for different time delays between laser pulse and x-ray pulse, information about the time development of the reaction can be gathered.

[1] Ligand = molecule or ion bonded directly to the metal center.

2 X-ray energy region

With photon energy roughly in the 1 to 100 keV (λ=1.2 nm to 12 pm) range, photon–matter interaction is dominated by the photoelectric effect; scattering of x-rays – both inelastic (Compton) and elastic (Rayleigh) – also plays a part, but much less, except in the lightest elements [5].

When absorbed owing to the photoelectric effect, the photon interacts with an electron in an atom, exciting the electron to an unoccupied orbital or removing it completely from the atom. As the unoccupied orbitals span a narrow region of a few eV just below the ionisation energy, the typical result is ionisation.

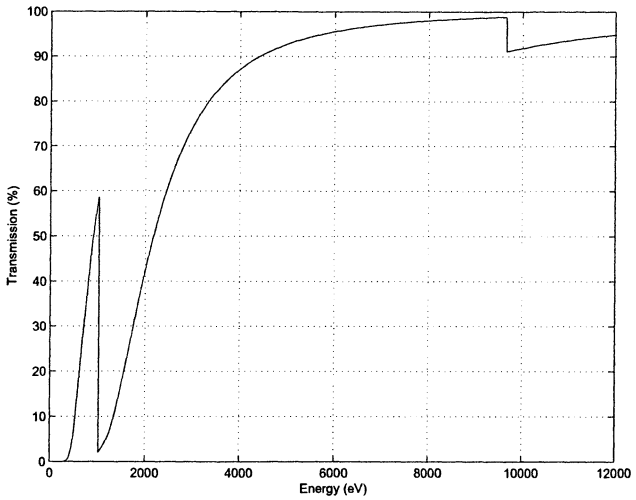

Figure 2: Simulated x-ray transmission of 0.5 μm Zn. The transmission dip at low energy (around 1 keV) arises because destination orbitals become reachable for L-shell electrons. This dip is referred to as the L-edge. For similar reasons, the dip just below 10 keV is called the K-edge.

Inversely, when an electron relaxes to an unoccupied place in an orbital, a fluorescent x-ray is emitted or an electron (an "Auger electron" [5]) is ejected. Recording either or both of these can be a complement to the x-ray absorption measurements. The energy of the x-ray fluorescence is characteristic of the element involved.

A simulated x-ray transmission spectrum for zink is shown in Figure 2. As is typical of such spectra, it shows an overall increase in transmission with increasing energy as well as strong discontinous decreases in transmission at certain energies. These decreases, which are called band edges, indicate that more ways in which absorption can occur are available. They occur whenever the photon energy attains the lowest value at which an electron in a given orbital can be excited.

The highest-energy band edge occurs when the energy is high enough to excite either of the electrons closest to the nucleus (n=1, the K-shell). Considerably less energy (approximately by a factor of ten) is required to excite the electrons in the next shell, the L-shell. Here, excitation can occur from three different orbitals (s, $p_{1/2}$ and $p_{3/2}$) with slightly different energies. These band edges are referred to as the L_I, L_{II} and L_{III} edges, respectively. Similarly, the orbitals in the M-shell give rise to five band edges at slightly different energies.

The lowest-energy band edge of a given element is the one caused by the excitation of an electron from the shell one step below the valence shell, and the energy of that band edge is the lowest energy required to excite the electrons to an unoccupied position above the valence shell. The edge energy is roughly proportional to the square of the atom number [3]. In Figure 3, the positions of the different band edges are plotted for the different elements. The x-ray absorption of an atom at a certain energy also increases strongly with the atom number. [3]

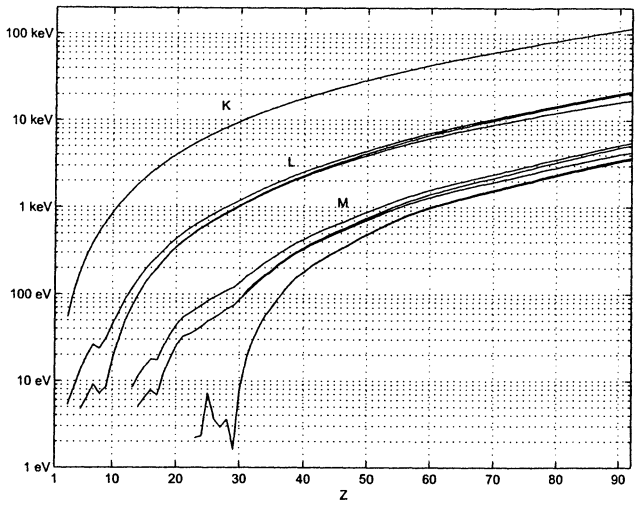

Figure 3: Positions of the band edges for the different elements. For each element, the K edge has the highest energy, followed by the L_I, L_{II} and L_{III} edges. At even lower energies, the five M edges appear. Data from [6].

2.1 Around the band edge

The energy region immediately surrounding the band edge is studied using XANES (x-ray absorption near-edge spectroscopy), and the region extending from the end of that studied using XANES (around 50 eV beyond the band edge) to around 1 keV beyond the band edge is called EXAFS (extended x-ray absorption fine structure). The exact limit between the XANES and EXAFS areas is not well-defined, but one possible definition is that XANES involves the discrete unoccupied orbitals while EXAFS deals with the continuum of states [3]. XANES is strongly sensitive to oxidation state and coordination chemistry (geometry of nearest neighbour atoms), while the EXAFS is more sensitive to the distances, and the species and number of neighbouring atoms [4].

Photon absorption in the EXAFS region is characterised by intensity variations caused by the outgoing photoelectron wave interfering with the waves backscattered from the surrounding atoms. The peaks in absorption represent those energies where the backscattered wave is in phase with the outgoing wave, and the valleys represent those energies where the two waves are out of phase [3]. This means that the EXAFS region can be studied to investigate the structure surrounding an atom, for example to determine bond distances.

In the XANES region, photon absorption depends mainly on the chemical state and the chemical environment of the atom or molecule. The characteristics of the absorption spectra are influenced by the energy levels of the lowest unoccupied molecular orbital (LUMO). One such characteristic relevant to this thesis is the oxidation state of an atom: when this changes, the band edges move slightly.

2.2 Information from the band-edge shift

Changes in absorption can be used to monitor a chemical reaction. When an electron is removed from an atom by a laser pulse, the oxidation state of that atom changes (its oxidation number increases by one). The resulting shift in band-edge position can be observed. There is a corresponding shift when an electron recombines. If there is a certain near-edge feature (as exemplified in Figure 4) in one of the oxidation states but not in the other, studying this is an even easier approach; however, such features are rare.

Band-edge positions for some metals relevant to this work are presented in Table 1. A complete

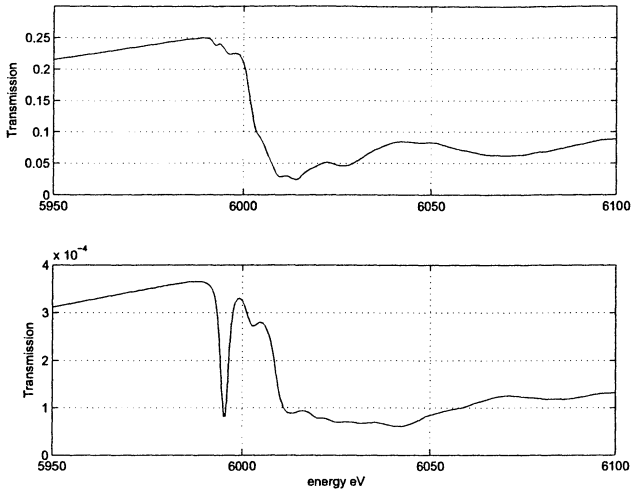

Figure 4: The K-edge of chromium in two different oxidation states, Cr(III) above and Cr(VI) below. The very obvious pre-edge absorption feature characteristic of Cr(VI) makes it easy to identify that oxidation state. Data from [7].

list of all K, L and M band edges for all elements is presented in Tables 2–5 in Appendix A.

2.3 Estimating the shift

When preparing an experiment in which the shift in band-edge position as the oxidation state changes is monitored, it is desirable to know how far the band edge is going to move, and what the resulting changes in absorption will be.

Steady-state measurements on the complex will provide the information about the ground-state position of the band edge. However, acquiring a steady-state spectrum of the excited state is more difficult, since the excited state might require laser excitation, and is also often available only for a short time.

For some reactions, it might be possible to drive the reaction to the excited state (and keep it there) using electrochemistry, making it possible to acquire a steady-state spectrum of the excited state.

For complexes where this cannot be done, a possible approximation is to use a complex similiar to the one that is going to be used in the experiment, but with a small modification to the ligands changing the oxidation number to match the one that the real complex would have in the excited state.

A rough approximation of at least the magnitude of the shift could be obtained using two complexes with the same metal centre atom as the complex intended for study, but with different ligands. These complexes are chosen so that the oxidation number of the first one matches the ground state of the real complex, and the oxidation number of the other matches the excited state of the real complex. Preferably, several different model complexes are used for each oxidation state, to see how much a change in ligands influences the shift.

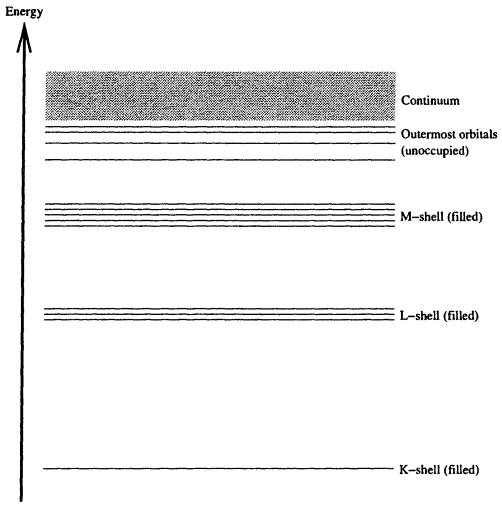

Figure 5: Principle representation of the photoelectric effect. When a bound electron absorbs a photon, the electron is either excited into the continuum as a free electron (photoemission) or excited to a higher-energy orbital. Band edges, which are named after the originating shell (K-edge, etc), appear when the photon energy has become large enough to place unoccupied orbitals within reach of electrons. Excitation into the outermost orbitals accounts for the fine structure near band edges.

3 Reaction candidates

In this section, some of the complexes are presented along with the associated reactions that it would be useful to be able to follow with time resolution.

Element	Edge	I [s]	II [$p_{1/2}$]	III [$p_{3/2}$]	IV [$d_{3/2}$]	V [$d_{5/2}$]
Ru (Z=44)	K	22117				
	L	3224	2967	2838		
	M	585	483	461	284	279
Re (Z=75)	K	71676				
	L	12527	11959	10535		
	M	2932	2682	2367	1949	1883
Os (Z=76)	K	73871				
	L	12968	12385	10870		
	M	3049	2792	2457	2031	1960

Table 1: X-ray band-edge energies (in eV) for the K, L and M edges of the metal centres of the complexes studied in this thesis. Data from [6].

3.1 CH_2I_2 isomerisation

The photo-dissociation of I_2 in CH_2Cl_2 ($I_2 \rightarrow I^\bullet + I^\bullet \rightarrow I_2$) has been studied using x-ray probing[8], and the isomerisation of CH_2I_2 is suggested as a possible candidate reaction that can be investigated using a similiar method.

The isomerisation that CH_2I_2 undergoes when excited by a laser is a reaction with well-known kinetics [9]:

$$CH_2I_2 \xrightarrow{h\nu} [CH_2I_2]^* \longrightarrow H_2CI^\bullet + I^\bullet \ (^2\Pi_{3/2} \text{ or } ^2\Pi_{1/2}) \longrightarrow H_2C^+\text{–}I^-\cdots I \tag{1}$$

$$H_2C^+\text{–}I^-\cdots I \rightleftharpoons H_2C=I^+\cdots I^- \tag{2}$$

$$H_2C^+\text{–}I^-\cdots I \xrightarrow{+I^\bullet} CH_2I_2 - I^\bullet \longrightarrow I_2 + \text{by-products} \tag{3}$$

Excitation requires a high photon energy (260 nm). The isomer product (Formula 2) is formed within 15 ps of laser excitation and is meta-stable, with a lifetime that depends on the solvent used [10]: 220 ns in CH_2Cl_2, 180 ns in n–C_6H_{14}, 45 ns in CH_3CN, 8 ns in ethanol and 5 ns in methanol.

The isomer then decays to I_2 and by-products. The actual percentage that decays to I_2 depends on the solvent and concentration used, but more by-products (for example, I_2^- and I_3^-) are formed in a polar solvent than in a non-polar solvent. As an example, 9.3 mM CH_2I_2 in methanol yields 50 % I_2.

An x-ray study of the reaction could use the fact that the I_2 absorption spectrum has a pre-edge feature [11] not present in I^-. By monitoring the appearance of this pre-edge, the decay can be studied.

3.2 Dye-based solar-cell reactions

A standard silicon solar cell is a p-n junction without external bias voltage. Each absorbed photon creates an electron and a hole. These charge carriers diffuse to the junction and are separated by the built-in electric field, producing a forward voltage across the barrier. This can be used to drive an external circuit [12].

In a dye-based solar cell, the functions of the light absorber and the charge-carrier transporters are separated. When n-type semiconductor materials such as TiO_2 are used, the dye molecule absorbs the photons, exciting electrons to the ligands of the dye molecule (metal-to-ligand charge transfer, MLCT). The electron is then injected from the ligands to the conduction band of the semiconductor. Subsequently, the dye molecule receives an electron transfer from a redox species[2] in the solution. This redox species is reduced at the counter electrode, forming a closed circuit [13].

Below, some complexes that can be used in a dye-based solar cell are presented. More data about these and similiar complexes are available in [14].

3.2.1 RuN3

There are several compounds based on a ruthenium central atom with different small ligands surrounding it.

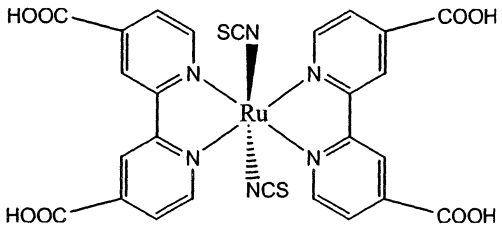

Figure 6: The RuN3 complex. When the molecule is excited (at around 800 nm), an electron transfer occurs from the ruthenium atom, through the aromatic ring and into the electron acceptor (for example, Ti in TiO_2) that is bonded to the carboxyl groups.

One complex commonly used in solar-cell experiments relating to artificial photosynthesis is known as RuN3 (Figure 6) [15].

On excitation, an electron transfer (ET) occurs from the ruthenium atom to the aromatic ligands, followed by relaxation to the electron acceptor (a molecule surrounding the RuN3 complex). For example, nanostructure TiO_2 particles in a film can function as electron acceptors. After a while, another electron recombines with the metal centre, allowing the reaction to happen again. In a solar cell, this movement of electrons would constitute the current source.

The electron movement in fact takes place in several steps [16]:

$$\text{Dye–SC} \xrightarrow{h\nu} \text{Dye}^{**}\text{–SC} \xrightarrow{ET} \text{Dye}^{+}\text{–SC}(e^{-}) \tag{4}$$

$$\text{Dye}^{**}\text{–SC} \xrightarrow{relax} \text{Dye}^{*}\text{–SC} \xrightarrow{ET} \text{Dye}^{+}\text{–SC}(e^{-}) \tag{5}$$

$$\text{Dye}^{+}\text{–SC}(e^{-}) \xrightarrow{BET} \text{Dye–SC} \tag{6}$$

In the above formulae, Dye is the RuN3 molecule, and SC is the semiconductor (TiO_2) that accepts the electrons. On absorption of light, the dye molecule is elevated to the excited state Dye**. In the

[2]Redox species = a species which can occur in more than one oxidation state in aqueous environments.

singlet-injection process (Formula 4), electron transfer to the semiconductor immediately follows as Dye** is deexcited. This is a very quick process, and the time between excitation and electron injection is much less than 500 fs.

Another process, triplet injection (Formula 5), also occurs. Here, the Dye** excited state relaxes thermally to the lower-energy state Dye*, from which the electron injection follows. This is a much slower process, on a timescale of approximately 100 ps.

After the electron injection, it is desirable that another electron should recombine with the positively charged dye, thus allowing the reaction to happen again so that an external current is produced. The electron that was injected can, however, sometimes move from the semiconductor back to the dye (Formula 6). Fortunately, this is a very slow process (μs to ms timescale), and there is a good chance of recombination from an external electron donator occurring before such back electron transfer (BET).

While this kind of reaction is easy to follow with a laser in the RuN3 complex, this is not the case for similiar but larger complexes. However, time-resolved XAFS could make it possible to study even the larger molecules, and such studies of the well-known RuN3 would be a good starting point for the studies of these larger complexes, since the results can be easily verified. Also, structural changes such as changes in bond length can be monitored by time-resolved XANES. This is not at all possible using a laser.

3.2.2 Blackdye

Another complex called Blackdye [17], similiar to RuN3 but with a slightly different ligand configuration (Figure 7), might also be interesting. Around 800 nm, the fundamental wavelength of the laser at D611, RuN3 has low absorption. Blackdye, however, has a much higher absorption at this wavelength owing to the different ligand configuration.

Blackdye is a well-known molecule, but the electron transfer has not been studied in detail because of problems with wavelength overlap between the electron acceptor and the relevant absorption feature of the blackdye molecule. As this is not a problem with time-resolved XAFS, this method could provide a possibility to investigate this molecule.

Like RuN3, the blackdye complex has carboxyl groups that enable attachment to a TiO_2 film.

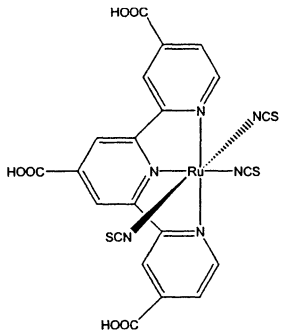

Figure 7: The blackdye complex. Even though blackdye is similar to RuN3, its slightly different ligand structure increases absorption at around 800 nm. Just like with RuN3, on excitation an electron transfer goes from the ruthenium atom to the aromatic ligands, and the electron subsequently relaxes to the electron acceptor bonded to the carboxyl groups.

3.2.3 Rhenium complex

There is a complex available which is similiar to the ruthenium complexes above, except that the ruthenium (Z=44) central atom is replaced by a rhenium (Z=75) atom (see Figure 8). The high x-ray absorption of such a heavy element makes it easier to achieve a large enough change in x-ray transmission in a time-resolved experiment. The complex with a rhenium metal centre has not been thoroughly investigated, but its behaviour with a ruthenium metal centre has been studied.

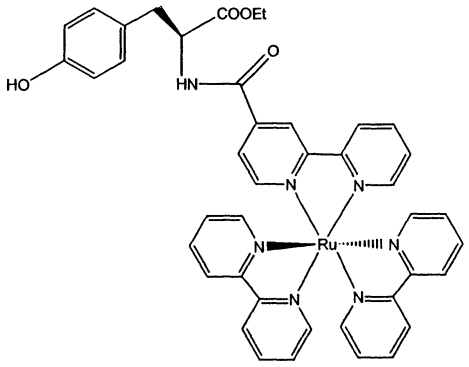

Figure 8: The ruthenium-tyrosine complex on which the rhenium complex is based. For time-resolved experiments, the ruthenium metal centre would be replaced by a rhenium atom.

Like for RuN3, the reaction scheme proposed for the ruthenium-based complex suggests that an electron is transferred from the metal centre to the ligands on excitation, and then injected into the TiO_2 conduction band. In this complex, however, an intramolecular electron transfer thereafter occurs from the tyrosine moiety to the excited metal centre, restoring the latter to a state similiar to the one before excitation. As a result of this final electron transfer, the tyrosine moiety undergoes tyrosyl-radical formation [18].

3.3 Osmium complex

Complexes similiar to the one shown in Figure 9 undergo interesting reactions when excited by light [19]. These complexes consist of various configurations of bridged ruthenium and osmium metal centres. On excitation, electron transfer occurs from one of the metal centres to another.

Depending on what laser wavelength is used for excitation, either the ruthenium or the osmium becomes the electron donator. On excitation, the electron moves to the ligands (MLCT) and then decays into a metal centre.

Since the metal centres are of different elements, it is possible to follow the band-edge shift in each metal centre independently of the other. Thus, the electron transfer can be seen from the perspective of both the electron donator and the electron acceptor.

The timescales of the electron transfer in the complex shown in Figure 9 are in the single ps region and thus too short for the time-resolved x-ray experiments discussed here. Modification of the bridging ligands can increase the duration of the electron transfer, possibly enough to enable such an investigation to be carried out.

The osmium L edges are around 11–13 keV, and the M edges are around 2–3 keV. Since the synchrotron photon flux is much larger in the 3 keV energy region than in the 11 keV region, it would probably be preferable to study the M edges. M edges have not been frequently used in steady-state XAFS/XANES experiments, so the shifts in band edge due to changes in oxidation state have not been thoroughly investigated. Still, there is no reason to believe that the M edge would not shift just like the K or L edges.

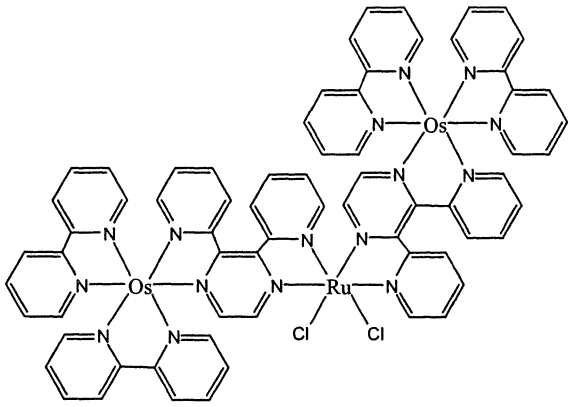

Figure 9: Example of an osmium complex. On excitation at a suitable wavelength, electron transfer happens from the ruthenium to one of the bridging ligands, from which the electron relaxes to the one of the osmium atoms. In an XAFS experiment, both the ruthenium band-edges and the osmium band edges could be monitored, showing the progress of the electron transfer from the perspective of both donator and acceptor atom.

4 Considerations relating to time-resolved setup

4.1 Light sources

4.1.1 X-ray source: the storage ring

When a moving electron changes direction, it emits radiation. If the electron speed is much lower than the speed of light, the angular distribution of the light emitted is very large. If, however, the electron is moving at relativistic speed, the angle of emittance becomes very narrow and light is emitted essentially only in the direction of the electron trajectory. The light emitted, which spans a very large region of wavelengths from far IR to hard x-ray, is, for historical reasons, known as *synchrotron radiation*. [20]

To produce x-ray light of the intensity required in the very narrow energy regions that are to be probed in this study, a storage ring must be used. In a storage ring, electron bunches are travelling at relativistic speed in a cyclic path. At various positions along the electrons' trajectory, light is emitted when they pass through a device that changes their direction. There are several types of such devices. The simplest one, the bending magnet, is used at beamline D611 at the MAX II ring – at which it would be possible to carry out the experiments whose feasibility this study investigates.

Moreover, the periodic pulsed structure of the x-ray light from the storage ring can be used to simplify and improve time-resolved measurements.

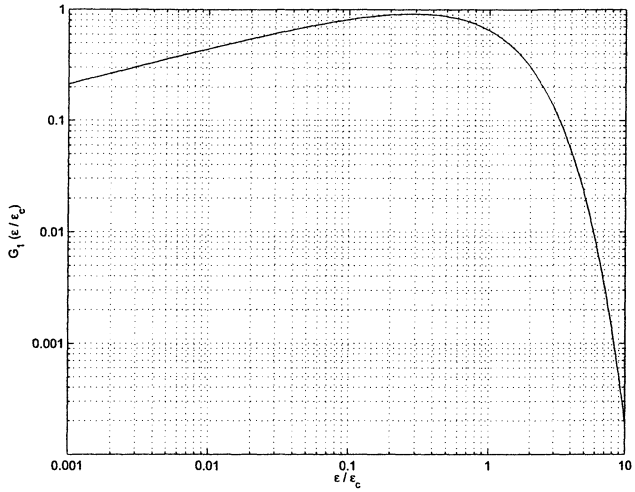

Figure 10: Plot of the $G_1(y) = y\int_y^\infty K_{5/3}(z)\,dz$ function, which describes the spectral distribution of bending magnet radiation. $K_{5/3}(z)$ is a modified Bessel function of the second kind. The parameter y is the value $y=\varepsilon/\varepsilon_c$, where ε is the photon energy and ε_c is the so-called *critical energy*, which divides the energy spectrum into two halves with equal emitted power. The maximum photon flux is slightly below the critical energy.

The electron flux from a bending magnet[21] can be written as

$$N(\varepsilon) = 1.256 \cdot 10^{10} \cdot \gamma i G_1(\varepsilon/\varepsilon_c) \tag{7}$$

where $N(\varepsilon)$ is the photon flux (photons/mrad·second) at 0.1% bandwidth
ε is the photon energy
γ is $E_e/m_{e_0}c^2$
ε_c is the critical energy (same unit as ε)
i is the ring current (in A)
$G_1(y)$ is a spectral distribution function (see Figure 10).

The Max II ring stores 1.5 GeV electrons at a current of at best 200 mA. At beamline D611, the critical energy ε_c = 2.3 keV. The light is emitted as 150 ps long pulses with a repetition frequency of 500 MHz [22]. The calculated spectral distribution of the light emitted is shown in Figure 11.

Beamline output is affected by a number of other factors.

If air enters the storage ring, its function will be disrupted. To prevent this, thin metal windows are used to shield the storage ring from the beamline. The x-ray absorption in these windows strongly influences the spectral distribution of the photons available at the end of the beamline. Figure 12 shows the spectral distribution after passage through the 120 μm of beryllium currently used at D611.

The flux is strongly influenced by the characteristics of the focusing optics and monochromator used. Also, it can be noted that the angular distribution of the x-rays from the bending magnet depends on the photon energy.

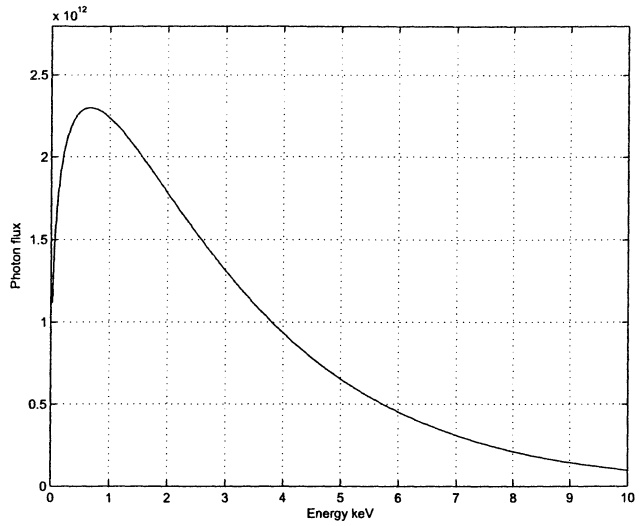

Figure 11: Photon flux at different energies for the bending magnet in beamline D611 at Max II (4 mrad, 10^{-4} band width). The plot was created using Formula 7 with ε_c=2.3 keV, i=170 mA, E_e=1.5 GeV.

4.1.2 Laser system

The core of the laser system at the Maxlab D611 beamline is a mode-locked titanium–sapphire cavity whose non-transmitting mirror is mounted on a piezo crystal. When the electric potential across the piezo crystal is changed, the size of the crystal changes, moving the mirror and altering the optical length of the cavity. Thus the repetition frequency of the cavity is controlled by the voltage across the crystal.

This is used to synchronise the output pulses from the laser with the 500 MHz Max II x-ray pulse train. The phase of the x-ray pulses is compared with the phase of the pulses from the laser. If the laser pulses arrive to early, the repetition frequency is decreased (by increasing the optical length) until the phase difference vanishes, and vice versa.

This laser design also makes it easy to change the delay between the pump pulse and the probe pulse: all that is required is the introduction of a phase delay into the laser-phase signal. Using such an arrangement, a resolution of a few ps and a range of a few ns can be achieved. Moreover, as no optical delay line is needed, the pump–probe delay can be changed very rapidly.

Next, in the amplification step, the output from the titanium–sapphire cavity is fed into an amplifier with a Pockels cell, which can be triggered by a maximum frequency of 10 kHz. Thus, only a very small fraction of the pulses of the incoming pulse train is amplified.

After the amplifier, the laser-pulse energy is around 1 mJ/pulse, at a wavelength of 800 nm. The pulse duration is about 30 fs.

4.2 Sample site

The sample site is the place where the two beams meet and the active molecules are located, e.g. because they are confined in some way. It can be designed in quite different ways, resulting in various trade-offs between simplicity of construction and handling, concentration of the active substance, achievable time resolution (relevant mostly when very short time intervals are to be studied) and losses in the laser pump beam and the x-ray probe beam. In order to obtain a complete and uniform excitation of the entire probed area, the laser pump-beam spot is chosen to be somewhat larger than the x-ray probe beam.

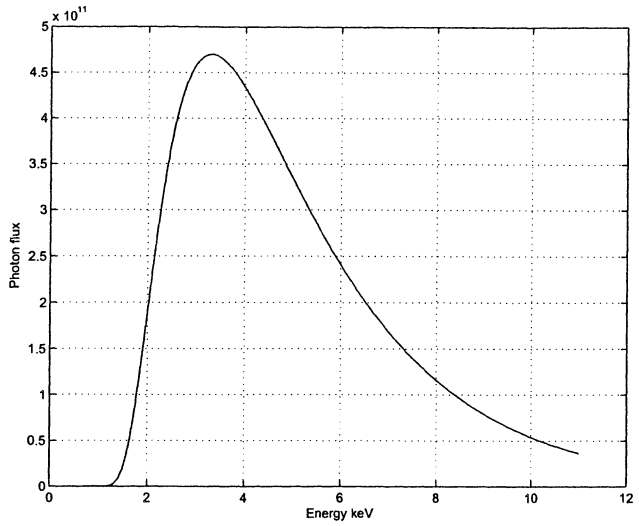

Figure 12: Calculated flux (photons/second, 10^{-4} BW) at various energies for x-ray photons originating from the bending magnet at Max II D611 (see Figure 11) and having passed through beryllium windows of a total thickness of 120 μm (see Figure 17 for beryllium transmission). The monochromator is assumed to have a transmission of 70% and the focusing mirror a transmission of 80%. The flux measured at 6 keV (see Section 7.1) is $2.3 \cdot 10^{11}$ photons/second. At other energies, the actual flux deviates more from this calculated flux (see Figure 36).

The active substance can be in solution or embedded into a thin solid film which is located on a substrate providing mechanical strength. The solution can either be kept in some kind of cuvette or be a freely flowing jet.

4.2.1 Jets

Jets have been popular in earlier time-resolved XAFS-experiments. The jet system is a closed system consisting of a pump, a container, piping, a jet nozzle and some kind of jet collector (often just a tube) that brings the liquid back into the system. While the volume of the system can be as small as 1.5 dl, a large amount of the active substance is still needed to achieve sufficient concentrations. In a realistic experiment, close to 10 g of complex would be needed.

It is worth noting that jets offer a convenient way of performing longer-timescale time-resolved experiments: the probe area is then located a few mm downstream from the excitation spot of the jet.

The only losses in a jet system come from absorption in the solvent. The drawbacks of a jet include its limited minimum thickness, the complications due to the pump system and the much larger amount of active substance needed.

4.2.2 Cuvette

In steady-state x-ray experiments, very simple cuvettes are often used. A simple method is to "dissolve" the active substance in some kind of grease or oil, and then form a cuvette by folding plastic sheets around it.

In a time-resolved experiment, the cuvette must meet higher requirements, since the width of the sample cell must be close to uniform and since at least one of the walls must be transparent at the laser wavelength.

One problem when making the cuvette is that the desired path length is typically a couple of hundred microns. This is difficult to achieve, especially since those walls that are sufficiently transparent in the x-ray region (at least below 4 keV or so) are thin and non-rigid.

Losses in a cuvette occur in the walls as well as in the solvent. However, the sample path length can be kept short, and by careful selection of the cuvette-wall materials, the losses can be kept acceptably low.

For more information about cuvettes, see the discussion about wall materials (Section 4.3).

4.2.3 Dispersion on a film

In some cases, the active molecules can also be confined inside a thin "film" consisting of TiO_2-particles with an average size of approximately 25 nm. The active molecules attach themselves to the surface of these particles. A rather high concentration of the active molecule can typically be achieved. The film itself is created on a substrate of some kind, which provides mechanical strength.

In other experiments, the substrates are often thin glass sheets, but those have undesirable x-ray properties and are thus unsuitable. Therefore the film would need to be created on another type of substrate, and a good candidate seems to be a sheet of a polymer such as Kapton (see below).

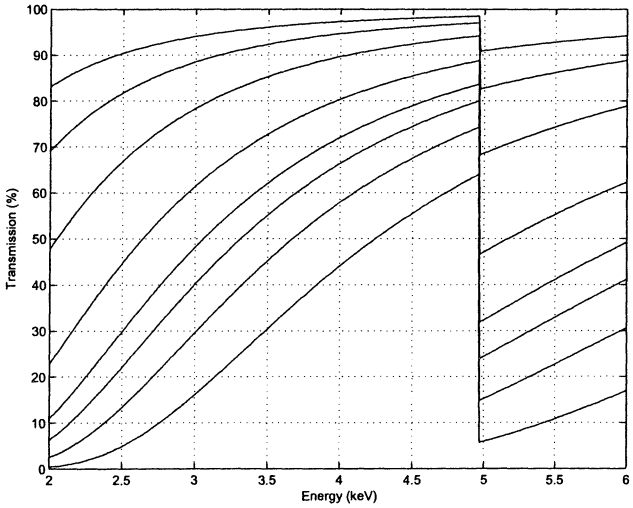

Figure 13: X-ray transmission of TiO_2 at 50% density (typical in a TiO_2 film) for different path lengths (1, 2, 4, 8, 12, 15, 20 and 30 μm). It is difficult to create a uniform film of a thickness greater than about 15 μm, but two films can be joined together to create a film of double the path length. At 4.966 keV the titanium K-edge appears.

The films are made by creating a uniform layer of a viscous dispersion of colloidal TiO_2 particles with a mean size of 25 nm on a substrate. The solvent is then allowed to evaporate, and afterwards the film is heated to approximately 450°C under air during 15 minutes. This heating removes an organic part of the solution that previously helped to keep the TiO_2 particles far enough away from each other to make the material porous. The resulting density of the TiO_2 film is about 50% of that of solid TiO_2.

The thickness of the resulting TiO_2 film depends on the thickness of the solution before it evaporates, on the concentration of the dispersion and on the size distribution of the TiO_2 particles. The above process can be performed repeatedly, creating a multi-layered film.

When the last part of the TiO_2 film is finished, the substrate (with the film attached to it) is lowered into an ethanol solution of the active molecules to allow these to diffuse into the film. Because of its original use in photo chemistry, this is referred to as *sensitising* the film. To speed up the process, the ethanol solution is heated slightly. Typical sensitising times for films are a few hours.

Having the active substance confined in a "film" located on a mechanically stabilising substrate is the option that produces the highest concentrations of the active substance, but not all reactions can be studied in a film. Furthermore, the substrate material must allow the film to be created on it, and materials meeting this requirement might have non-desirable properties in terms of x-ray absorption. However, the laser beam does not actually have to pass through the substrate, and as the substrate is only on one side of the sample, the x-ray losses are reduced.

4.3 Window and wall materials

The materials used at the sample site have to meet several requirements. One side of the cell must let both x-rays and laser light in, and both sides must be sufficiently transparent to x-rays. The material must not interact with the active molecules nor with the solvent used, and it must be able to withstand the intense laser pulses without melting or deforming. Additional properties, such as mechanical rigidity and high heat transmission to remove heat from the sample, are highly desirable.

4.3.1 Kapton

One of the most promising materials for windows and film substrates is Kapton. Also known as polyimide, it is a polymer with the sum formula $C_{22}N_2O_5H_{10}$ and the structure shown in Figure 16. Since it contains only light elements, it has a low absorption in the x-ray region – a 7.6 μm Kapton film has over 60% transmission at 2 keV and over 90% above 4 keV (see Figure 14).

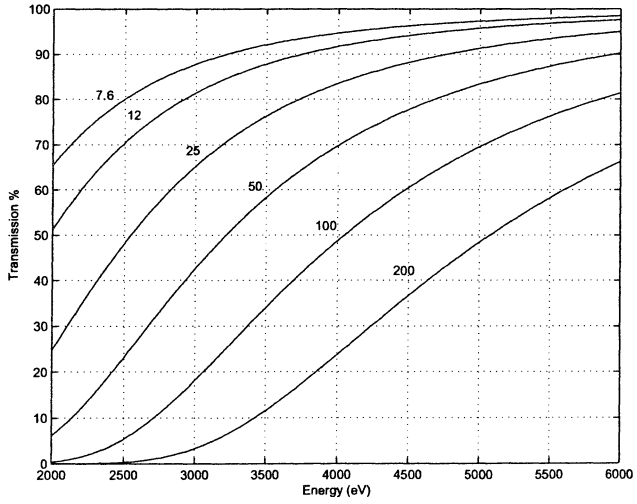

Figure 14: Transmission of Kapton sheets of some commercially available thicknesses (7.6 μm up to 200 μm) in the hard x-ray region.

In the visible region, absorption is still acceptably low for a thin film, especially in the long-wavelength region above 570 nm where transmission even for a 12.6 μm film is 80% or greater (Figure 15). Thus it might be feasible to let the pump beam in through a Kapton window.

The material is very strong, and sheets as thin as 7.6 μm are easy to handle and can be stretched to create a uniform surface. Other good properties of Kapton include its high degree of chemical

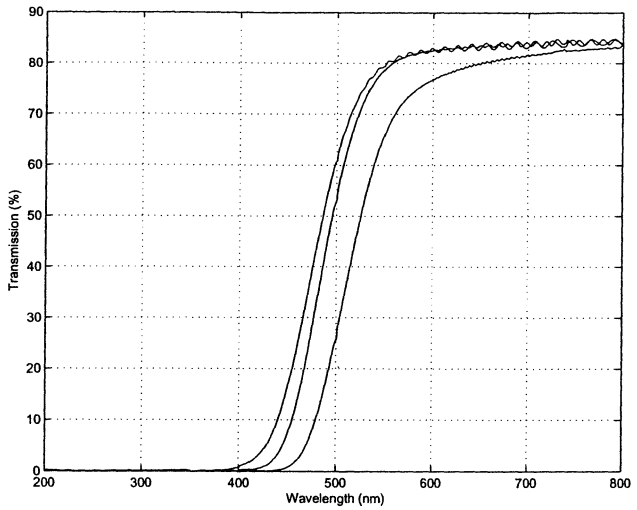

Figure 15: Transmission of thin Kapton sheets in the visible region. From left to right, samples are 7.6, 12.7 and 25.4 μm commercially available Kapton sheets. The oscillatory patterns in the 600–800 nm region are artefacts due to interference effects from reflection of light on the surfaces of the film. These interference patterns can be used to determine the thickness of a film.

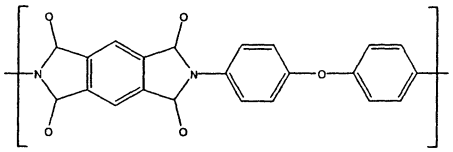

Figure 16: Kapton, $C_{22}N_2O_5H_{10}$, 382.33 g/mol, 3.74 mol/l, is a brownish-yellow polymer. Its very high mechanical strength, heat resistance and chemical inertness, along with its low absorption in both the x-ray and the visible region, make it well suited for the experiments considered here.

inertness, the lack of any known organic solvent and its high resistance to ionising radiation. Its high temperature stability (230°C steady state, 400°C temporarily) helps avoiding problems due to heating from the laser. Kapton also differs from many other common polymers in that it does not absorb helium gas and thus can be used in a helium atmosphere.

In addition, a TiO_2 film can be created on the Kapton. Because of the high temperatures used during the annealing phase of film creation, this is not possible with other commonly available polymers.

Because of these suitable properties, Kapton has been a frequent choice in steady-state x-ray experiments using simple setups [23, 24].

Kapton is trademarked, patented and manufactured by DuPont, and is available in a great many different shapes. It is commercially available in very thin (down to 7.6 μm) sheets.

4.3.2 Polypropylene

Polypropylene, which has a lower absorption in the x-ray region than Kapton and which is essentially transparent in the visible region, could have been an excellent window material. Unfortunately, the mechanical properties of polypropylene are such that it is difficult to use it as a cuvette wall or to create a uniform surface on it. Further, it has much lower heat stability, making it likely to deform or melt when heated by a laser. Moreover, it would not be possible to create films (e.g.

TiO_2) on it using the method described earlier, since the heat in the annealing phase would melt it.

4.3.3 Beryllium

Beryllium is frequently used as a window material in synchrotron-radiation systems and is therefore readily available as very thin sheets. Because of its low atom number (Z=4), it has low absorption in the x-ray region (see Figure 17).

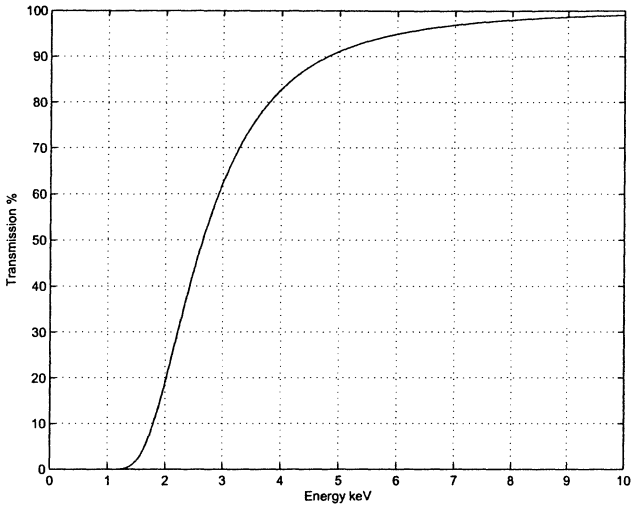

Figure 17: X-ray transmission of 120 μm beryllium. Because of its low absorption at high energies, beryllium is often used in protective windows along the beamline.

As beryllium is intransparent in the visible region, it cannot be used for the front window. However, it might be considered as a film substrate or for the "back" window in a cuvette. Further, depending on the laser wavelength, its reflective properties may double the effective length of the pump path.

As a metal, beryllium has good heat-conduction properties that might help avoiding sample degradation due to heating from the beams. Also, its high melting point (1287 °C) makes it possible to anneal a TiO_2 film on a beryllium surface.

Even thin slices (in the region of 100 microns) of beryllium have sufficient mechanical strength for a uniform film surface to be easily obtainable. Unfortunately, beryllium is strongly toxic and must be handled with care. For instance, fumes from vaporisation due to laser heating would have to be safely removed.

4.4 Detection

To detect photons, several different devices can be used, e.g. an avalanche photodiode or a streak camera.

4.4.1 Avalanche-photodiode array

In an avalanche photodiode (APD), the incoming photons produce electron/hole pairs just like in a standard P-N photodiode. However, before the charge carriers generated are collected, the released electrons are accelerated by an external electric field (a reverse bias of up to 2 kV). The electrons acquire a high enough energy to release secondary electrons via ionisation when they

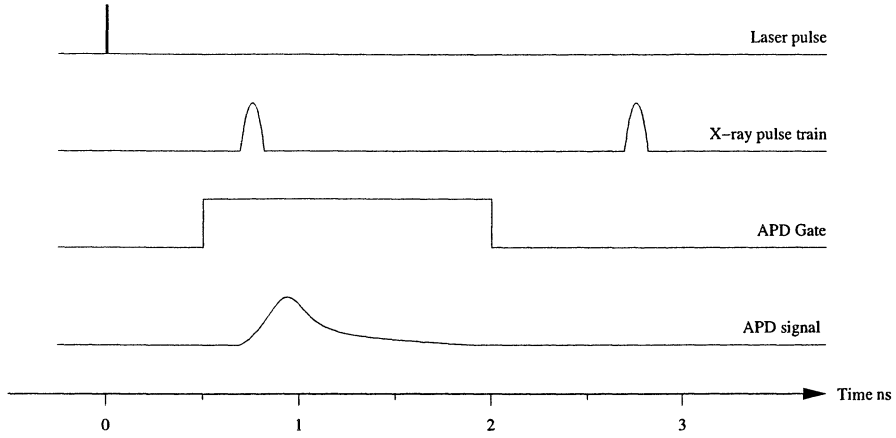

Figure 18: Nanosecond-scale time-resolved measurements using an APD. By exploiting the pulsed structure of the x-rays — short bursts separated by a time long enough to allow the APD to decay — a resolution roughly equivalent to the width of the x-ray bursts can be obtained. The signal from the APD is only collected when the gate signal is active. Different time intervals are probed by changing the delay between the laser pulse and the x-ray pulse that occurs when the APD gate is active.

collide with the atomic lattice. The secondary electrons, in their turn, are accelerated enough to cause further ionisation. The end result is an avalanche of electrons released for each electron/hole pair produced; thus there is a high built-in gain in the APD.

An APD typically allows a time resolution of 1 to 100 ns, but special APDs offer close to 0.1 ns resolution [25]. The pulsed structure of the x-rays can be exploited to increase the resolution to roughly the length of the pulses (see Figure 18).

One option could be to use a photo-multiplier tube (PMT). Compared with a PMT, the main advantages of an APD are better quantum efficiency (up to 90%), lower noise and higher linearity. The main advantage of a PMT over an APD is its higher gain.

4.4.2 Absolute photon-flux measurements

An APD can be used to measure the absolute photon flux. When operated in the low-bias region (approximately 50V), it has no gain and works like any silicon diode. The photon flux can be approximated for a silicon-based detector using the following empirical formula:

$$\text{released electrons} = \text{A(E)} \cdot \text{incoming photons} \cdot \frac{\text{photon energy (eV)}}{3.6\,\text{eV}} \tag{8}$$

where A(E) is the absorption of the APD silicon substrate at the current photon energy.

4.4.3 Streak camera

To achieve a time resolution in the single ps region, a streak camera can be used. In a streak camera, the incoming photons hit a photocathode and cause back-side emission of photoelectrons. The electrons are accelerated, focused and guided towards a phosphorus screen, which when hit emits fluorescence light. The electron beam is continuously moved to cover different parts of the screen, and the resulting image can be captured by e.g. a charge-coupled device (CCD) camera.

To monitor the fastest reactions dealt with in this thesis, a streak camera would be required. Unfortunately, the streak camera has a very low quantum efficiency: 0.1% at 10 keV and 10% at 100 eV are realistic values [22]. A method of estimating the quantum efficiency is presented in [26].

5 Simulation

To describe photon absorption in matter, the Beer–Lambert law is often used:

$$T = e^{-n \cdot \mu_a \cdot x} \tag{9}$$

where T is the transmission
n is the number of atoms per volume unit (m^{-3})
μ_a is the absorption coefficient (m^2)
x is the path length (*m*).

Chemists often use a "more practical" form instead:

$$T = 10^{-\varepsilon \cdot c \cdot d} \tag{10}$$

where T is the transmission
ε is the extinction coefficient ($M^{-1}cm^{-1}$)
c is the concentration (M)
d is the path length (*cm*).

Conversion between μ_a and ε is done as follows:

$$\varepsilon = \frac{10 N_A}{\ln 10} \mu_a \tag{11}$$

where N_A is the Avogadro number.

5.1 X-ray transmission

Since this thesis deals mainly with those changes in transmission that occur as the oxidation state of an atom is changed, the following terminology is useful. In the complexes studied here, the excitation of a complex molecule often leads to an increase in the oxidation state of the metal centre. As discussed earlier, this causes a shift of the band-edge position towards higher energies. Thus, if the x-ray probe is fixed at a certain energy just above the band edge, the transmission of the atom will increase when it is excited, as the band edge will be shifted away from the probe energy region.

Therefore, the transmission just above the energy of a band edge is referred to as the "ground-state x-ray transmission" and the energy *just below* the position of the band edge is referred to as the "excited-state x-ray transmission" *at the same energy as the ground-state value.* That is the absorption that will occur at the energy of the probe once the band edge has shifted.

Below, then, $\varepsilon_{xag}(E)$ is the x-ray extinction coefficient at energy E, while $\varepsilon_{xae}(E)$ is the *excited-state* x-ray extinction coefficient at energy E. In this model, $\varepsilon_{xae}(E)$ equals $\varepsilon_{xag}(E - \Delta E)$, where ΔE is the shift in band-edge energy due to the oxidation-state change.

The Beer–Lambert law has been used to determine the x-ray absorption of the candidate complexes and the solvent. The transmission of the complex can be written as

$$T = 10^{-d(\varepsilon_{xs}c_s+\chi c_a\varepsilon_{xae}+(1-\chi)c_a\varepsilon_{xag})} \quad (12)$$

where T is the transmission
d is the path length (cm)
ε_{xs} is the x-ray extinction coefficient of the solvent ($M^{-1}cm^{-1}$)
ε_{xag} is the x-ray extinction coefficient of the active molecule when in ground state ($M^{-1}cm^{-1}$)
ε_{xae} is the x-ray extinction coefficient of the active molecule when excited ($M^{-1}cm^{-1}$)
c_s is the concentration of the solvent (M)
c_a is the concentration of the active substance (M)
χ is the fraction of active molecules excited

Of special interest here is the relative change Π in transmission that occurs when a certain fraction of the active molecules is excited. For example,

$$T(\chi=0.85) = \Pi \cdot T(\chi=0.12) \quad (13)$$

where Π is 1.07, would be referred to as a relative increase of the transmission by 7% when the excitation level of the active molecules is increased from 12% to 85%

This is the method that has been used to generate all simulations of x-ray transmission and of changes in x-ray transmission after excitation. Calculated extinction coefficients can be downloaded from [27]. As these are theoretical data, they provide no details about band-edge structure, only a rough idea of the absorption before and after the band edge as well as the location of the band edge itself.

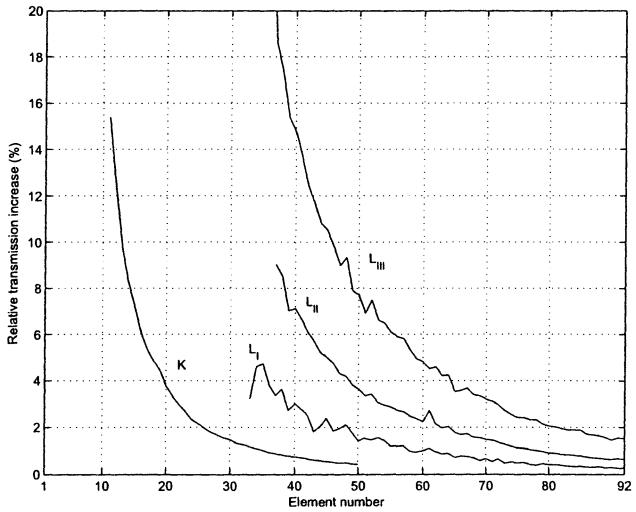

Figure 19: *Relative* change in transmission at the K and L band-edges for 10 mM concentration of the different elements in 1 mm path length. Even though these are simulated data, a few general trends can be seen that would probably be confirmed by experiments.

Calculated values for relative band-edge changes from these data deviate from actual results for two practical reasons.

First, the real absorption differences are often larger just around the band edge. Second, the real band edge is not completely vertical, and the shift might not be enough to move entirely from maximum absorption to minimum absorption, which means that the entire range of absorption

difference is not available.

The first effect skews the simulation towards showing too small a change, whereas the second has the opposite effect.

5.2 Laser excitation

To calculate what fraction of the active molecules is excited by the laser pulse, the Beer–Lambert law cannot be used directly. This is beacuse of an underlying assumption in the derivation of this law: that the molecules can be excited over and over again. During the short laser pump pulse (femtosecond timescale), however, the active molecules can be excited only once. Owing to the large number of photons available in the high-power laser pulse, direct application of the Beer–Lambert law often indicates that the total number of photons absorbed is larger than the total number of active molecules.

In the subsequent calculations, it is assumed that the excitation leads to a long-lived energy state, and that no stimulated emission occurs.

The adaption of the Beer-Lambert law chosen here to ensure that the fraction excited can be calculated involves dividing the photons entering the sample into smaller bunches ($N_{in}^{(1)}$, $N_{in}^{(2)}$, ..., $N_{in}^{(N)}$). For each photon bunch, the number of photons absorbed is then calculated (Formula 14), and the concentration c of the absorbing molecule is correspondingly decreased (Formula 15). If the excited state also absorbs photons, the corresponding concentration is increased, etc. This is repeated until all incoming photons have been sent through the sample, and the output photons ($N_{out}^{(1)}$, $N_{out}^{(2)}$, ..., $N_{out}^{(N)}$) are then summed up.

$$N_{out}^{(k)} = N_{in}^{(k)} \cdot 10^{-d \cdot \varepsilon \cdot c^{(k)}} \tag{14}$$

$$c^{(k+1)} = c^{(k)} - \frac{N_{in}^{(k)} - N_{out}^{(k)}}{N_A \cdot V_{cell}} \tag{15}$$

Here, V_{cell} is the volume, in m^3, of the part of the sample that is excited. In an obvious model, this is a cylinder whose length is that of the sample cell and whose radius is that of the laser beam.

When a pulse of photons impacts upon a highly absorbing molecule such as the complexes considered in this thesis, the photons are initially absorbed mainly in the front part of the sample cell. Thus, it is a good idea also to discretise the path length, treating each part as a separate sample cell. In that way, an excitation profile of the entire sample cell can be obtained. To simplify analysis of the results, it is desirable to achieve quite uniform excitation (i.e. the front part of the sample cell should not have a much higher excitation level than the rear part).

6 Simulation results

It is necessary to find out what the relative band-edge absorption change will be when the material is excited by a certain laser energy. This can be used to calculate the actual changes in the number of x-ray photons from each storage-ring bunch passing through the sample before and after it is excited.

The x-ray beam cross-section is a fixed parameter. Often, the smallest available beam size is chosen. This determines the size of the laser beam to be used: the laser beam should be somewhat larger than the x-ray spot, so that the area to be probed is completely and rather uniformly excited. It seems reasonable for the radius of the laser beam to be double that of the x-ray beam, and this is the relation used in this thesis.

The laser-region extinction coefficient of the excited active molecules is typically not known, and it is assumed to be zero. This is obviously rather optimistic, but possibly reasonably close to the actual value for quite a few complexes.

It is also assumed that the lifetime of the excited state is much longer than the laser pulse (otherwise, the probing results would be useless anyway), so that each active molecule absorbs only once. Moreover, it is assumed that no stimulated radiation occurs when a photon interacts with an excited molecule.

6.1 An earlier experiment

An experiment similiar to those investigated here is presented in [28]. In this experiment, $Ru(bpy)_3$ was excited with a 400 nm 300 μJ laser, increasing the oxidation state of Ru from II to III. After excitation, the complex decays with a lifetime of 300 ns.

Parts of the conditions of that experiment have been simulated here (see Figure 20) using the same technique as the one used elsewhere in this thesis. Since that previous experiment was successful, it is useful for comparisons.

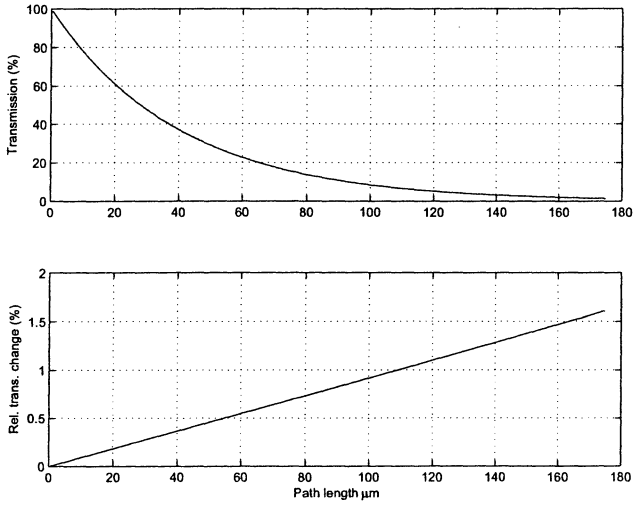

Figure 20: Change in x-ray transmission at the Ru L_{III} edge (2838 eV) as *10%* of the $Ru(bpy)_3$ molecules are excited. The $Ru(bpy)_3$ concentration is 80 mM, in H_2O. This is a simulation of the expected conditions for a time-resolved experiment that has already been carried out [28]. In that experiment, a 0.1 mm pathlength was used.

6.2 CH_2I_2

The isomerisation of CH_2I_2 would be an interesting reaction to study. For this reaction to occur, a short photon wavelength (around 260 nm) is required. At D611, photons of approximately this wavelength (267 nm) can be generated as the third harmonic of the 800 nm laser. Unfortunately, the low conversion ratios of the laser system and the rather low absorbtion of CH_2I_2 make it difficult to obtain an excitation fraction large enough to be monitored. See Figures 21 and 22 for simulations of excitation and the resulting change in x-ray transmission for some realistic values of laser power and path length.

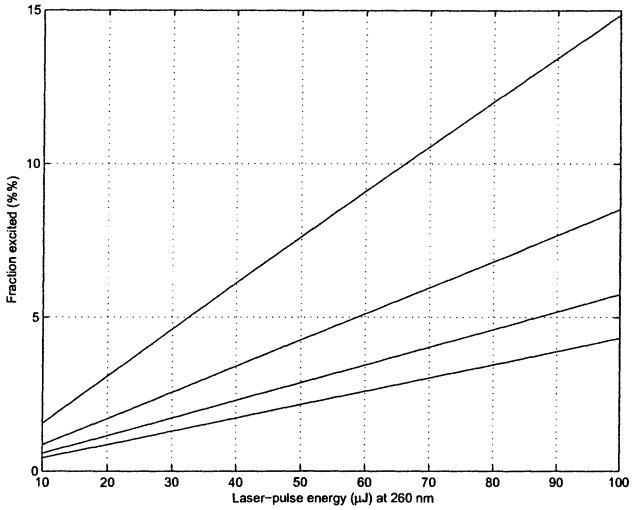

Figure 21: Resulting excitation of 100 mM CH_2I_2 in methanol for path lengths 100 (upper graph), 200, 300 and 400 (lower graph) μm. The radius of the laser spot is 200 μm. Note that only 50% of the excited molecules (assuming the same result as for 9.3 mM CH_2I_2 solution) enter the relevant excited state, which means that the effective excitation fraction is only half of that shown by this figure.

As can be seen in Figure 21, with the given setup and the possible path lengths, it is difficult to achieve an excitation fraction much higher than approxinmately 15%. The resulting change in x-ray transmission (Figure 22) is too low to be easily detected. Note that in the CH_2I_2 only about half of the molecules excited actually enter the stage where the oxidation state has changed.

6.3 Blackdye

Blackdye is a ruthenium complex that has been modified (by changing its ligand structure) to shift its absorption maximum towards longer wavelengths (i.e. closer to the 800 nm fundamental laser wavelength available at D611). The simulation in Figure 23 shows that laser power is not a problem in that situation, and that a sufficient excitation fraction is easily obtained at moderate laser-pulse energies.

Since 90% excitation is easily achieved for blackdye, it is interesting to see what the corresponding change in x-ray transmission is. That is shown for the L_{II} and L_{III} edges of ruthenium in Figures 24 and 25.

6.4 Rhenium complex

In [18], 15 μM of the complex and 120 μM of TiO_2 in water was used. Here, it is assumed that the ratio 1:8 of complex to TiO_2 can be generally used, is used for higher concentrations. In Figure 26,

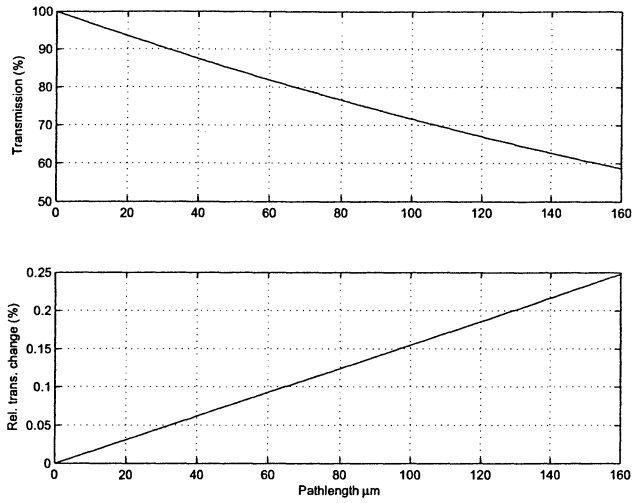

Figure 22: Change in x-ray transmission at the I L_I edge (5188 eV) as 10% of the CH_2I_2 molecules are excited. The concentration of CH_2I_2, in methanol, is 100 mM. The results obtained by measuring the pre-edge feature mentioned in [11] are likely to give similiar changes in absorption.

the results around the Re M_{IV} edge (1949 eV) are shown for 12 mM of complex.

For edges at higher energies, the absorption change around the band edge is smaller, and at the Re M_{III} edge at 2367 eV (Figure 27) a higher complex concentration (40 mM) is needed to achieve reasonable transmission changes.

Higher energies are interesting as well. The simulation around the Re L_{III} edge at 10535 eV (Figure 28) shows interesting results. X-ray transmission is high, and acceptable changes can be seen with 40 mM complex concentration. Note that the optical properties of this complex (the Ru in the original complex substituted with Re) are unknown, and that the assumed excitation level of 90 % might be unrealistic.

6.5 Osmium

The osmium complexes are promising as well. The M-edges are at low energies, but the M_I edge, with the highest energy, is the most interesting one (Figure 29). Since it turned out that the high energy of the Os L_{III} edge was within reach of the equipment, a simulation of the conditions of that edge is included as well (Figure 30).

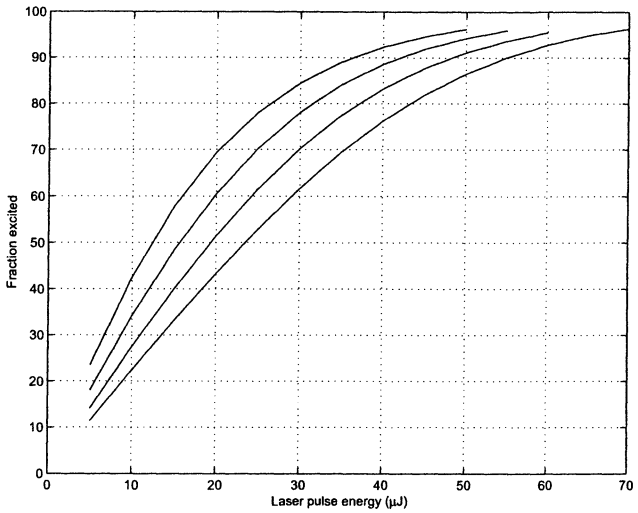

Figure 23: Resulting excitation of the Blackdye complex for different path lengths (15, 30, 45, and 60 μm) using a 800 nm laser. The beam radius is 100 μm and the Blackdye concentration is 147 mM, a value that has been achieved experimentally earlier. It is assumed that no relaxation happens during the pulse. Since the Blackdye complex is nearly transparent, the pulse energy required to achieve a certain excitation fraction does not increase much as the path length increases. The Blackdye is assumed to be in a 50% density TiO_2 film in which no laser absorption takes place.

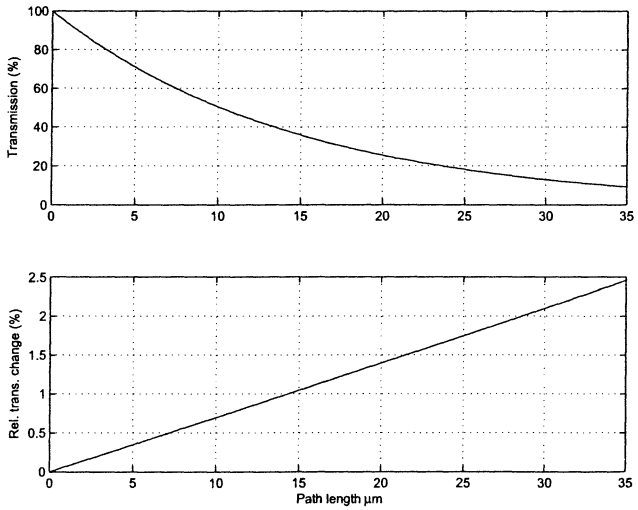

Figure 24: Change in x-ray transmission at the Ru L_{II} edge (2967 eV) as 90% of the blackdye molecules are excited. The blackdye concentration, in a TiO_2 film (50% density), is 147 nM.

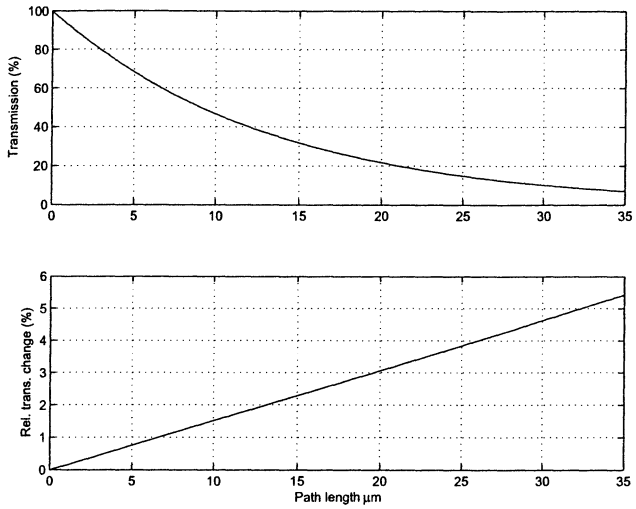

Figure 25: Change in x-ray transmission at the Ru L_{III} edge (2838 eV) as 90% of the blackdye molecules are excited. The blackdye concentration, in a TiO_2 film (50% density), is 147 nM.

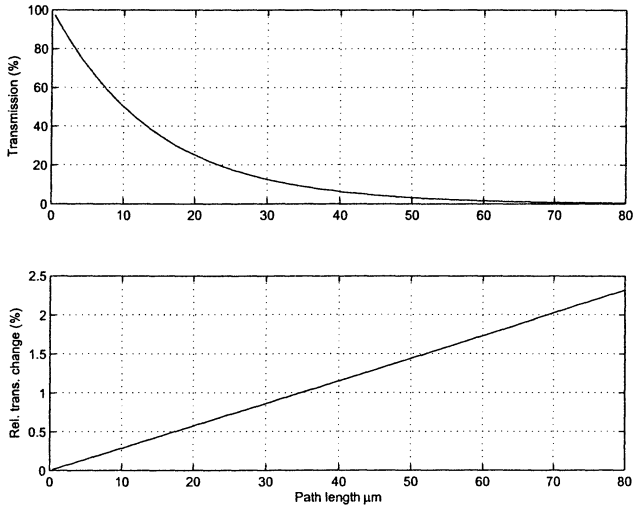

Figure 26: Change in x-ray transmission at the Re M_{IV} edge (1949 eV) as 90% of the molecules of the rhenium complex are excited. 12 mM of rhenium complex and 96 mM of TiO_2 in H_2O.

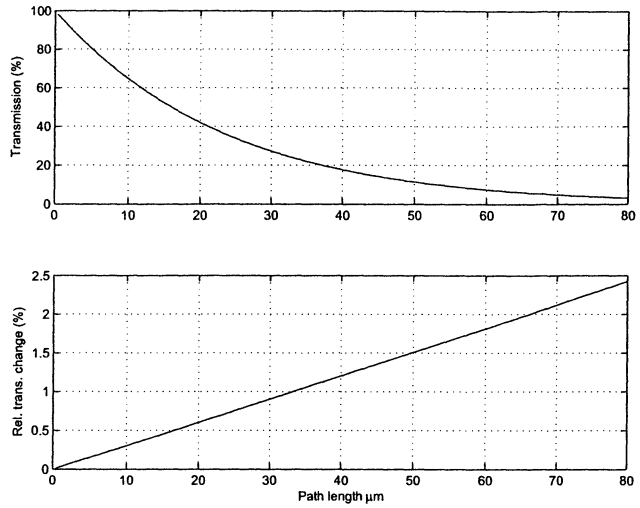

Figure 27: Change in x-ray transmission at the Re M_{III} edge (2367 eV) as 90% of the molecules of the rhenium complex are excited. 40 mM of rhenium complex and 320 mM of TiO_2 in H_2O.

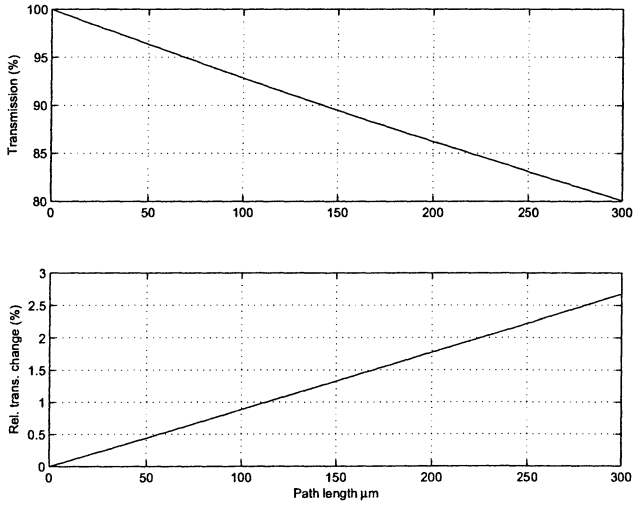

Figure 28: Change in x-ray transmission at the Re L_{III} edge (10535 eV) as 90% of the molecules of the rhenium complex are excited. 40 mM of rhenium complex and 320 mM of TiO_2 in H_2O.

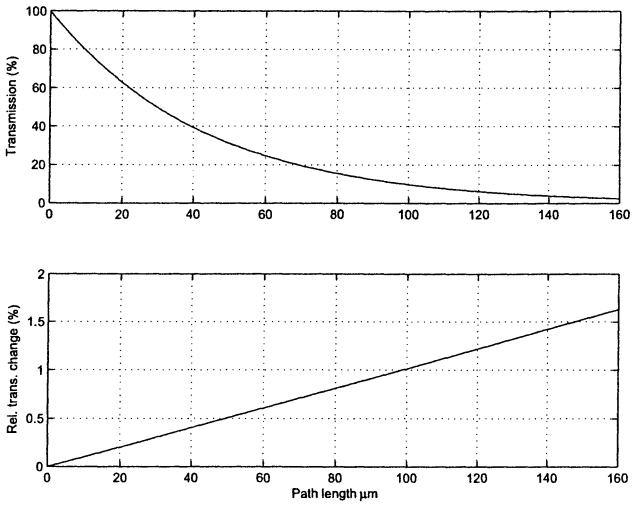

Figure 29: Change in x-ray transmission at the Os M_I edge (3048.5 eV) as 90% of the OsRu2 molecules are excited. The OsRu2 concentration, in H_2O, is 40 mM.

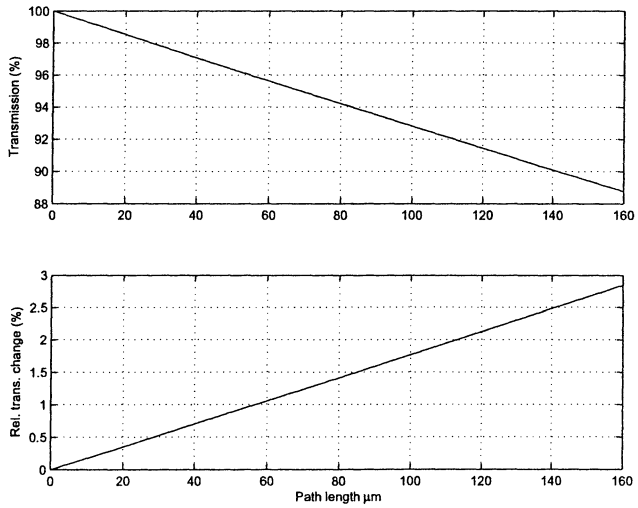

Figure 30: Change in x-ray transmission at the Os L_{III} edge (10871 eV) as 90% of the OsRu2 molecules are excited. The OsRu2 concentration, in H_2O, is 40 mM.

6.6 Solvents and windows

The x-ray absorption of the solvent, the sample-site walls and the surrounding atmosphere all decrease the number of available photons, especially at lower energies (say, less than 5 keV) where x-ray absorption is generally high.

The high absorption of air makes it advantageous to perform the experiments in vacuum. Apart from this, however, it would be preferable if the experiments did not need to be performed in vacuum, as this not only makes changing samples more complicated and cumbersome, but also causes problems with evaporation of samples dissolved in liquids.

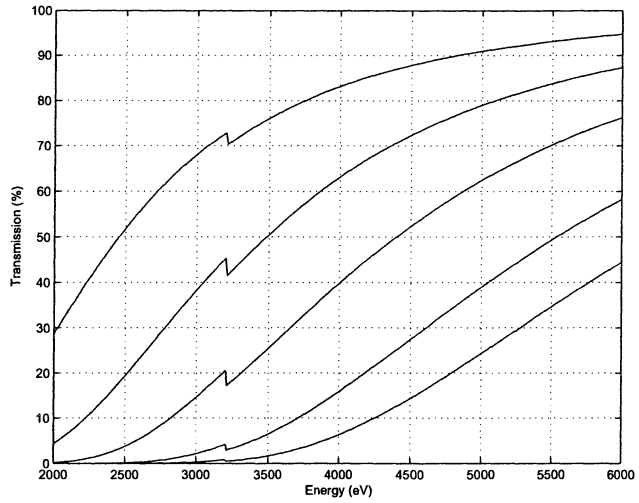

Figure 31: X-ray transmission of air at room temperature (298 K) and normal pressure (101325 Pa) for different path lengths (2, 5, 10, 20 and 30 cm). The dips seen at 3203 eV represent the K band-edge of the 0.934% Ar typically found in ambient air.

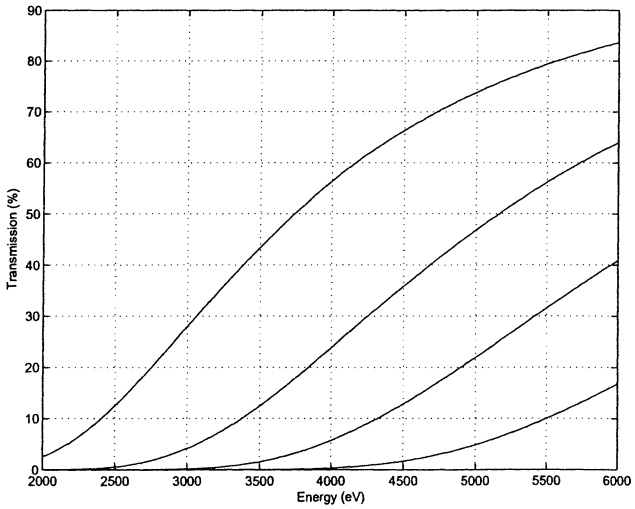

Figure 32: X-ray transmission of glass (SiO_2, 36.8 M) for different path lengths (10, 25, 50 and 100 μm). It appears that glass slides thick enough to be easily handled would have an unacceptably low x-ray transmission.

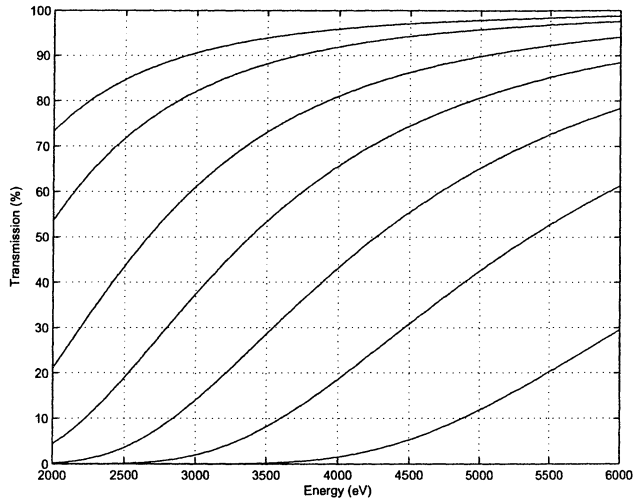

Figure 33: X-ray transmission of H_2O for different path lengths (5, 10, 25, 50, 100, 200 and 500 μm).

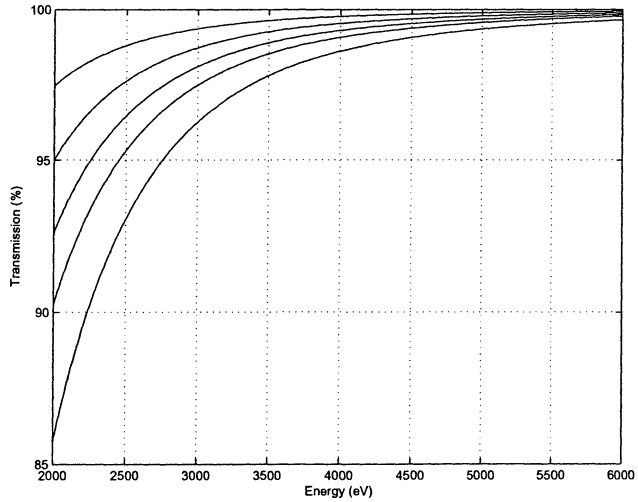

Figure 34: X-ray transmission of helium at room temperature (298 K) and normal pressure (101.325 kPa) for different path lengths (25, 50, 75, 100 and 150 cm). Clearly, helium absorbance in the x-ray region can be ignored.

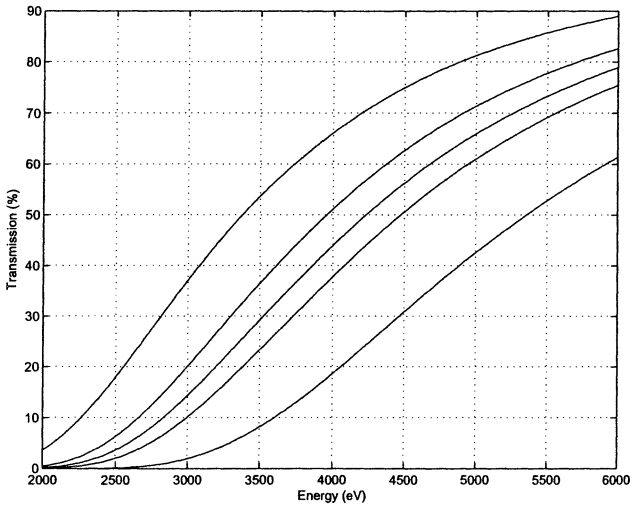

Figure 35: X-ray transmission of different solvents for 200 μm path length (a rather reasonable path length for a cuvette experiment). In order of decreasing transmission: *n*-hexane, acetonitryl, ethanol, methanol and H_2O.

7 Initial experiments at D611

Two types of initial experiments were performed at D611: measurements of photon flux and of steady-state conditions.

7.1 Photon-flux measurements

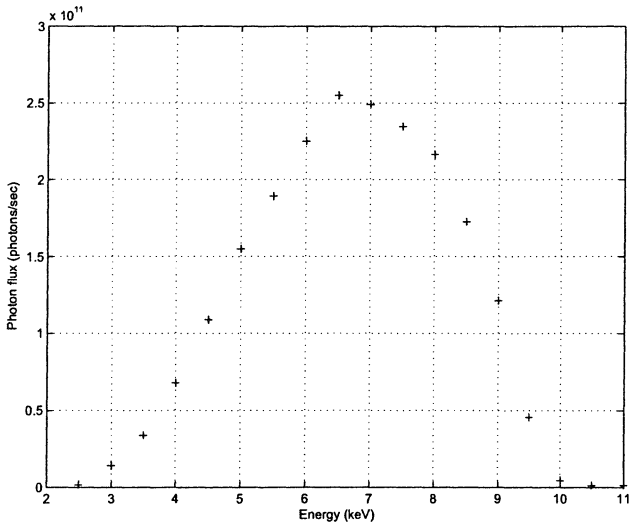

Figure 36: Actual photon flux at various energies from the Max II D611 beamline measured using an APD with a 10 μm Si substrate. These values were measured using a 32 mm air gap before the detector and a storage-ring current of around 170 mA. For each energy, the monochromator was manually optimised to provide the maximum possible photon flux. At 2.5 keV, the flux is $1.8 \cdot 10^9$, at 10 keV $4.5 \cdot 10^9$, at 10.5 keV $1.3 \cdot 10^9$ and at 11 keV $1.4 \cdot 10^9$ photons / sec.

To measure the photon flux, an APD operated in the low-bias region was used and the photon flux calculated according to Formula 8. The APD used a substrate of 10 μm silicon.

At 6 keV, a current of 17 μA was measured, corresponding to a photon flux of $2.3 \cdot 10^{11}$ photons/second. At 10.5 keV, the current measured was 40 nA and the corresponding flux $1.3 \cdot 10^9$ photons/second. More results are shown in Figure 36.

7.2 Steady-state spectra

To collect steady-state experimental data, as well as to determine what transmission changes could realistically be resolved using the APD detector, a tentative setup was used. In this setup, the sample was positioned, in air, a few centimetres after the monochromator output window, and the detector was placed as close as possible to the sample, leaving an air gap of a few millimetres.

7.2.1 Data collection

Data-collection equipment (with associated software) to scan a range of energies was already available at D611, but this was not at all designed for collecting a high-resolution spectrum – rather, it was used to take a rough scan of energies for other purposes, such as calibrating the monochromator.

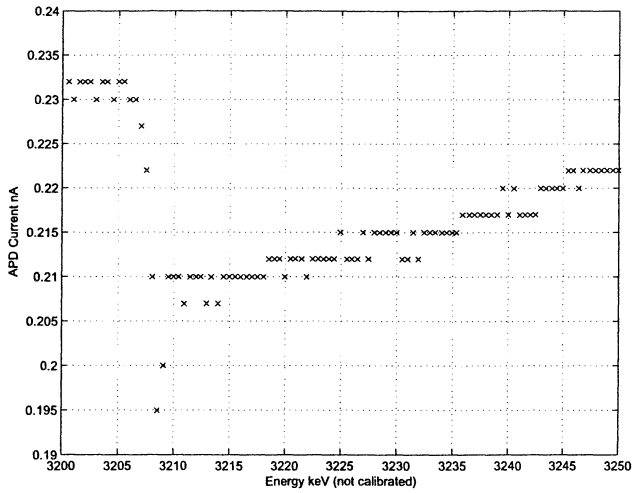

Figure 37: This measurement, using the initial data-collection equipment, shows the absorption around the Ar K-edge in an air path of approximately 5 cm. The quantisation problems (i.e. too big steps) are clear. According to Berkeley data, the theoretical transmission decrease here is around 10%.

A test result using the existing equipment can be seen in Figure 37. It shows the transmission decrease around the Ar K-edge in an air path of approximately 5 cm. While it is clear that the detector can resolve the edge, it is also obvious that the resolving power of this equipment is severely limited by the large quantisation steps of the A/D converter. This is due to a mismatch between the input-signal range and the A/D range: the A/D converter has a range of ± 10 V (with a resolution of 8192 points), whereas the maximum detector preamp output is 2 V.

The preamp in question (a picoammeter) can use only amplifications of powers of ten, and thus it was often possible to use only a small part of the full 0–2 V range. There were no postamps available to amplify from 2 to 10 V. Moreover, the changes to be resolved were in the 10 % range. Taken together, this means that the A/D converter range actually used is often close to only 1/1000 of the full range.

Obvious improvements to the data-collection system thus include an amplifier with finer gain settings as well as some kind of offset addition to move the measurement baseline closer to the middle of the A/D range. However, no such equipment was available during the beamline time allotted. Instead, the data-collection system was reprogrammed to read data directly from the picoammeter. This enabled initial steady-state experiments to be carried out. In a time-resolved experiment, though, this kind of setup cannot be used.

The higher resolution and internal averaging available from the picoammeter proved to be very good, and the quantisation problems were resolved. A transmission graph of the Ar K-edge can be seen in Figure 38.

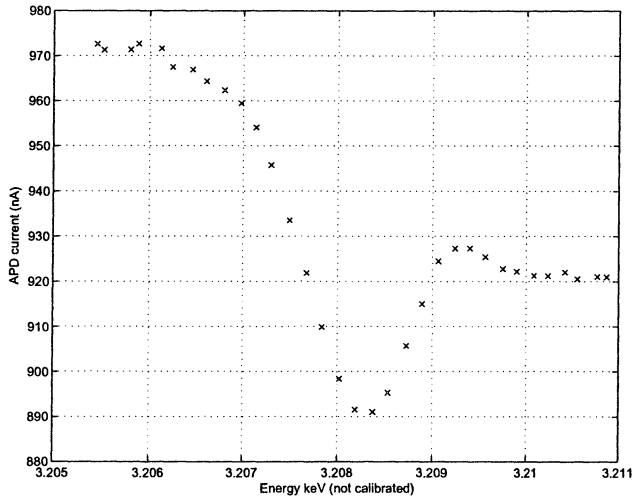

Figure 38: The Ar K-edge in an air path of approximately 5 cm, measured using the new data-collection equipment. Averaging is performed internally in the picoammeter over 20 samples. Clearly, the discretisation problems have been resolved.

7.2.2 Detector and monochromator

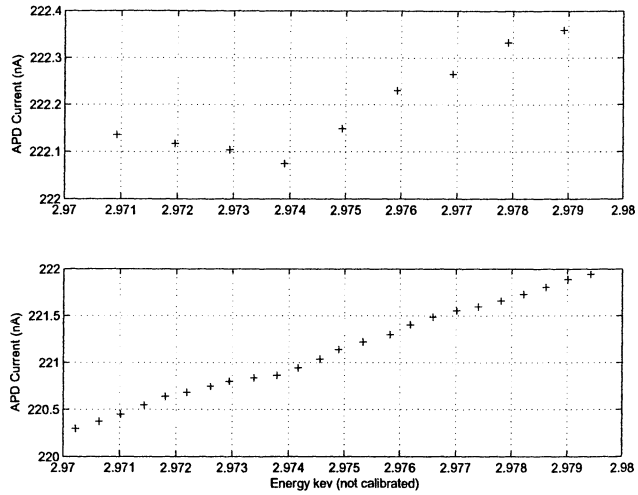

Figure 39: Two scans at the Ru L_{II} edge (RuN3 in TiO2). In the upper diagram, a dip in transmission can be clearly seen at approximately the energy expected. Unfortunately, the dip vanished – as shown by the lower diagram – when the step size was decreased in order to achieve better resolution of the peak. This is explained by the detector ramping.

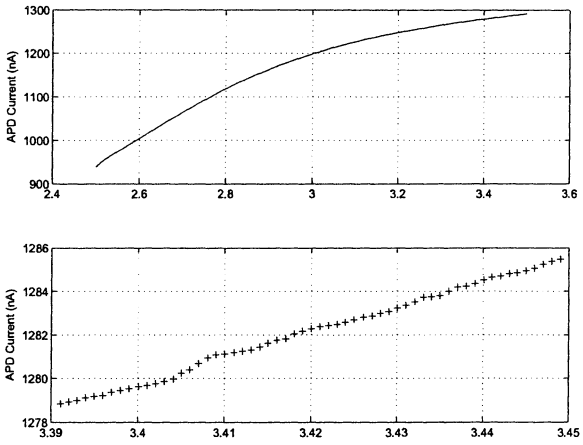

Figure 40: This figure shows detector ramping. For this scan, the x-rays were *turned off*, so the x-axis is really just a time axis. The whole scan took about an hour. The lower plot, which is a randomly selected magnification of part of the upper plot, shows short-timescale ramping behaviour. As can be seen, this is rather non-uniform and thus not easily compensated for.

To investigate the Ru L_{II} edge, a thick film of RuN3, made according to the description given in Section 4.2.3, was inserted into the system. It was assumed that the ruthenium-complex concentration would be the same in the thick film as in the thin film. Then the transmission change at the band edge would be comparable to that at the Ar K-edge.

Figure 39 shows two attempts at resolving the Ru L_{II} edge. As can be seen, the transmission dip is much smaller in the lower – higher-resolution – scan, and the whole higher-resolution spectrum shows a steady, almost linear, increase in transmission.

To investigate further, the x-rays were turned off and a spectrum was collected. This was expected to be a straight line with some detector noise. Instead, the result shown in Figure 40 was obtained.

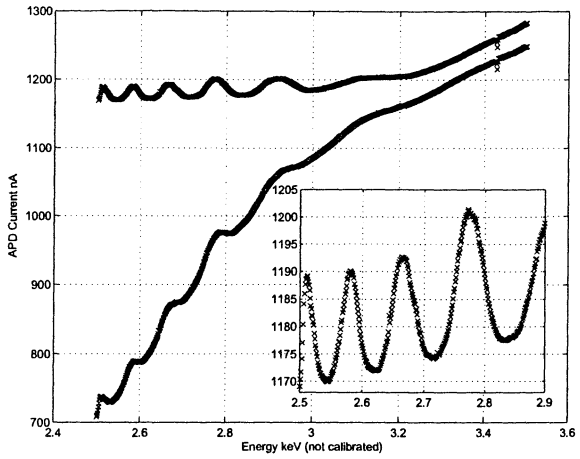

Figure 41: Intensity variations caused by the monochromator in the low-energy regions. Two consecutive scans were made; the differences between them are largely due to detector ramping. At 3.43 keV, a monochromator glitch can be seen in both scans. To show the monochromator-induced variations more clearly, a magnification of the 2.5–2.9 keV region of the second scan is included in the bottom-right part of the figure.

This slow, uneven increase could go on for hours and was slow enough to be difficult to discover, yet large enough to hide small peaks. In the higher-resolution spectrum mentioned earlier, which took longer to collect than the lower-resolution one, this ramping effect was very apparent and actually concealed the band-edge decrease.

Another problem in the collection of steady-state spectra is illustrated in Figure 41. The large oscillatory peaks are due to (unexpected) monochromator effects. This problem could be eliminated if some means could be introduced to measure the x-ray intensity after the monochromator but before the sample.

Some experiments seem to indicate that the monochromator may not always have assumed the position requested – being off by a few electron volts –, especially for high energies around 10 keV. This is quite understandable, since such energies are beyond the claimed range of the monochromator.

The detector and data-collection system could not correctly image the band edges, owing to the ramping and monochromator problems, even though they were well capable of detecting them.

7.2.3 Results

Measurements of band-edge transmission changes with large intensity variations, such as those shown in Figures 42 and 43, tended to have an adequate resolution.

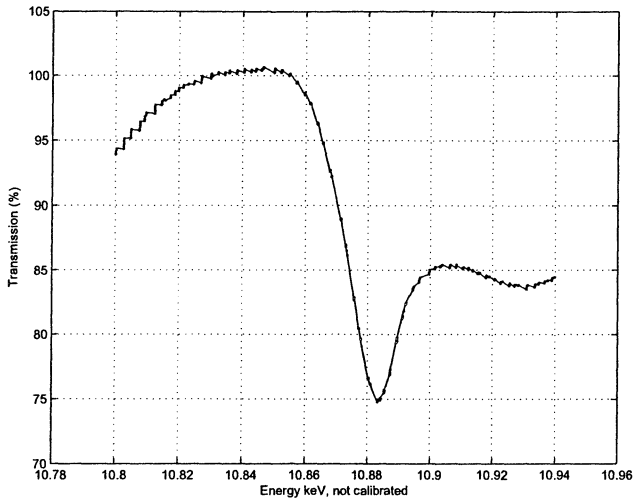

Figure 42: This graph shows the absorption from the Os metall centre around the Os L_{III} edge in the $Os(IV)Cl_6K_2$ complex. The apparent low transmission at the beginning is likely due to the very non-linear ramping after the detector voltage has just been turned on.

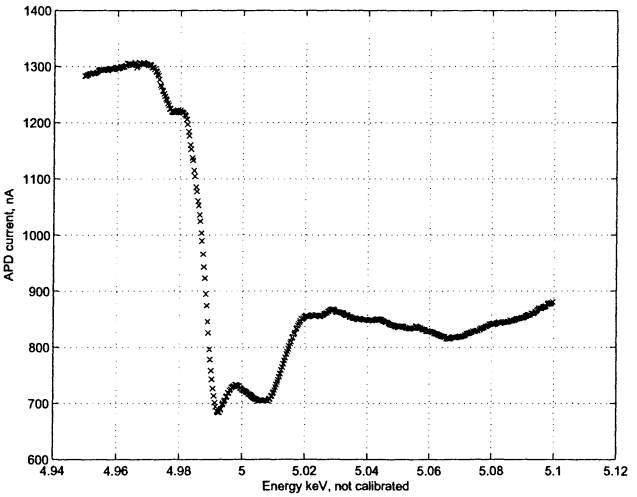

Figure 43: The titanium K-edge in a TiO_2 film, very well resolved. This edge could possibly be used to study changes in Fermi-energy level of TiO_2 particles in connection with electron transfer from dye molecules.

8 Experimental results from ELSA

To investigate the earlier problems, the same samples were remeasured at the dedicated XAFS setup at the ELSA (Electron Stretcher Accelerator) 3.5 GeV synchrotron facility in Bonn.

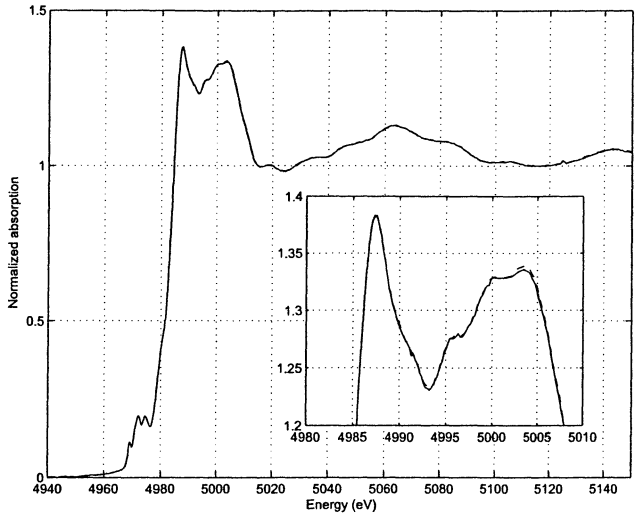

Figure 44: Two scans of the Ti K-edge from a film of 9 nm TiO_2 particles recorded at ELSA. This graph shows the high degree of reproducibility that can be achieved at a dedicated XAFS setup.

The XAFS part of the setup used two ionisation-chamber detectors to measure the x-ray intensity before and after the sample. The measurements were taken in vacuum. Instead of Be windows, 8 μm Kapton windows were used, allowing measurements at lower energies than would have been possible with Be.

In the graphs from ELSA, the spectra have been normalised. The spectra show absorbance. For normalisation, a line is fitted to the background absorption before the band edge, and this fitted background is subtracted. After that, the spectrum is scaled so that a line fitted to the background after the band edge is located at unit absorption.

Figure 45 shows the results for the Ru sample. Compared to the Ru L peak in [28], this peak is much larger.

Figure 46 shows measurements of two osmium model compounds, one with Os(III) and one with Os(IV).

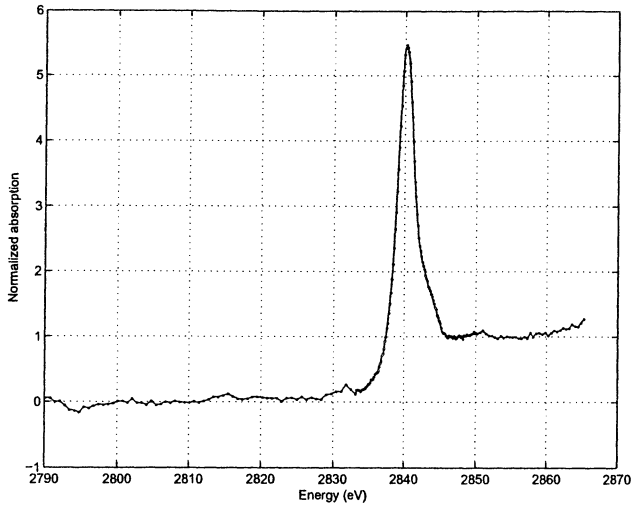

Figure 45: The Ru L1 edge, measured at Bonn on the very same sample earlier unsuccessfully measured at D611 at Maxlab. The sharp peak would make time-resolved measurements possible even with a rather small shift in wavelength as the oxidation state changes.

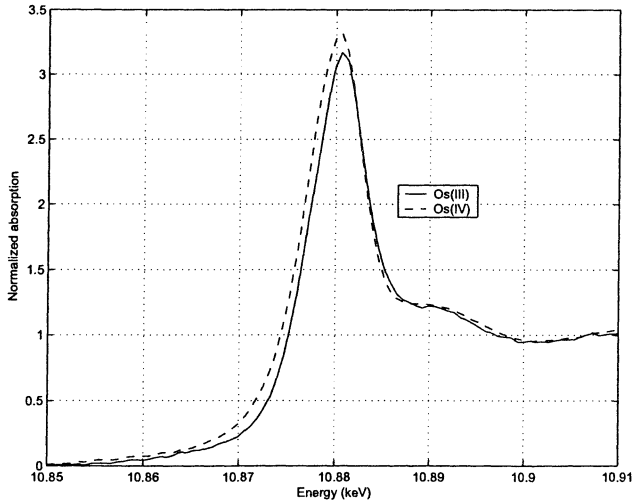

Figure 46: Normalised data for two osmium measurements in Bonn. Two model compounds were used, $Os(IV)Cl_6K_2$ and $Os(III)Cl_3(dpp)$. As can be seen, in this well-resolved graph, in the higher oxidation state the peak is broadened towards lower energies. The typical shift in peak position towards higher energies is not seen. This is assumed to be because of differences in the two compounds used, and clearly shows that it is difficult to draw any conclusions about the band-edge shift that will occur.

9 General conclusions

9.1 Photon-flux considerations

For the time-resolved experiments, a high photon flux is of the utmost importance. Owing to photon losses in solutions and the smallness of the change in transmission to be monitored, the actual decrease in the number of photons is very low. This is a problem especially for rapid reactions, where the time intervals must be short. Fortunately, the heating effect and resulting sample degradation from the monochromated x-ray beam is insignificant, so the choice of photon flux is not limited by sample considerations.

In Section 7.1, the photon flux at D611 at 10.5 keV was found to be $1.3 \cdot 10^9$ photons/second. As mentioned in Section 4.1.1, the x-ray flux is pulsed. With a repetition frequency of 500 MHz, each pulse on average contains 2.6 photons.

With a laser-repetition frequency of 5 kHz, 5000 samples can be taken each second, resulting in an average flux before the sample of 13000 photons per second. Owing to a 75% loss of photons in the sample and a 95% loss due to detector inefficiency, around 160 photons per second are actually collected.

Integrating 10 seconds per discretisation point, some 1600 photons would be collected. This ought to make it possible to follow transmission changes of a few percent. With a pulse length of 150 ps, a useful interval would be 3 ns (twenty 150 ps steps). This can be scanned in 200 seconds, suggesting that it would be feasible to perform such an experiment.

Trying to resolve at picosecond timescale using a streak camera, the photon flux turns out to be far too low at 10.5 keV. With a bunch length of 150 ps, and 2.6 photons per bunch, 0.017 photons are available each ps in each bunch. With 5000 measurements per second, the result is 85 photons collected per ps interval per second. This is assuming, optimistically, that there are no losses in the sample. The efficiency of the streak camera is very low, around 0.1 % at 10 keV. Thus, each second, only 0.085 photons are detected per ps interval. This is clearly far too little for this experiment to be feasible.

At 6 keV, with $2.2 \cdot 10^{11}$ photons/sec, each bunch contains 450 photons, and thus 3 photons/ps. Assuming that there are 50% losses in the sample, the measurement rate of 5000/sec results in the collection of around 15000 photons per second per resolved ps interval. Although somewhat better at 6 keV than at 10 keV, the low efficiency of the streak camera is still a major problem. Assuming a streak-camera efficiency of 0.2%, 15 photons are detected each second. Collecting data for 60 seconds, each interval yields 900 photons, and a 50 data-point scan would take 50 minutes. Even without taking into consideration additional losses, this appears to be a difficult experiment to carry out.

9.2 Laser-energy considerations

Obviously, a high laser-pulse energy is preferable, so that as large a fraction of the active molecules as possible will be excited. However, even though the x-ray energy that would be deposited in the sample did not appear likely to cause sample degradation, ordinary laser radiation easily would. To reduce these problems, it is desirable to choose a laser wavelength for which the absorption of the active molecule is very large. Also, the active molecule could be slightly altered (e.g. modification of ligand structure) to move the absorption maximum so that it matches the laser wavelength better.

9.3 Other considerations

A standard IR sample cell was investigated as to whether it could be used to stabilise the cuvette and to provide an easy method for adding the solution. There turned out to be problems with solution leaks at the short path lengths used. The best method for cuvette construction discovered so far is to make a small hole through an object of the desired thickness, the *spacer*, and then to glue or tape the cuvette walls to the hole ends.

To investigate the resistance of Kapton in the laser wavelength region, a Kapton sheet was irradiated by a 540 nm laser (5 kHz, 8 mW) with a small beamsize (less than 1 mm diameter) for several hours. No visible changes could be observed in the Kapton after this treatment.

A problem with jets is that so large quantities of active molecules are required. In a realistic experiment, close to 10 g of complex would be needed, while typical yields of small-scale synthesis are around 200 mg.

Drawbacks of the CH_2I_2 experiment include the high laser-photon energy required for excitation, and the large number of different products formed in the reaction. It would be easier to follow a reaction with a single well-defined end state.

The very large and sharp Ru L_I peak (Figure 45) of RuN3 in TiO_2 that was measured at ELSA makes time-resolved experiments based on this molecule look very promising. Thanks to the sharpness of the peak, even a very small shift of the peak would result in a considerable change in absorption. The difference in peak height compared with the Ru peaks in [28] is remarkable and explained by the different ligands and environment (TiO_2 vs. H_2O).

No Ru L peak could be seen at D611 (see Figure 39). The fact that the very same sample gave the result shown in Figure 45 when measured at ELSA demonstrates that there were no problems with the sample.

In Figure 46, osmium from two model compounds has been measured. As can be seen, instead of shifting towards higher energies, the peak is broadened when the oxidation number increases from 3 to 4. This shows that extrapolation from model complexes must be used with care when drawing conclusions about peak shifts.

The calculated photon flux (Figure 12) and the measured photon flux (Figure 36) do not match very well. This is partly because the transmission of the monochromator and the focusing mirror depends on the energy of the photons. The calculated values are useful for rough estimations, though.

10 Summary

10.1 Photon flux

For a time resolution of 150 ps, an APD can be used, and its very good photon economy makes it reasonable to assume that experiments can be carried out with a photon flux not much lower than 10^8 photons/sec.

For ps scale time resolution, a streak camera is required, and its poor photon economy makes the photon flux at a bending-magnet beamline such as D611 too low for experiments to be easy to carry out even at optimal photon-flux energies. The realistic photon flux required seems to be in the 10^{12} photons/sec range, to a large extent depending on streak-camera efficiency at the energy used.

10.2 D611

The photon flux at D611 appears to be sufficiently high for 150 ps time-resolution experiments using an APD within a large range of energies – up to around 10.5 keV.

The high photon flux that would be required for ps scale time resolution using the D611 streak camera is not available at D611.

At least some of the following modifications to the D611 beamline would improve the feasibility of time-resolved experiments:

- Improving the monochromator positioning accuracy in the high-energy region (roughly above 10 keV);
- Measuring beam intensity before the sample (I_0 measurement);
- Eliminating APD ramping;
- Modifying the data-collection system to work in a time-resolved experiment.

10.3 Reactions

CH_2I_2: Since this is a reaction that is well known and for which the mechanisms are well understood, it is well suited for initial investigations of the possibilities of a time-resolved x-ray experiment as the results can be easily verified using existing theory.

Since the lifetime of the decay to be monitored depends on the solvent, a solvent resulting in a lifetime that fits the experimental setup well can be chosen. Since the smallest amount of by-products are formed when using a non-polar solvent, such a solvent is preferable in order to simplify the evaluation of the experiment.

The laser energy presently available at D611 at the required wavelength (this would be the third harmonic, at around 266 nm) is not sufficient for a time-resolved investigation.

RuN3: The back-electron transfer can be monitored at the 150 ps resolution provided by the APD setup. Triplet injection could be monitored using a streak camera at a beamline with higher intensity than D611. Singlet injection, however, is too fast to be monitored. The present laser setup at D611 cannot excite a large enough fraction of this complex. The very high and sharp Ru L_I peak in RuN3 makes the absorption changes likely to be very large.

Blackdye: The blackdye complex is similiar in chemistry to the RuN3 compex, but less well investigated with regard to time scales of reactions. Its much higher absorption around the fundamental wavelength of the laser at the D611 setup makes it realistic to excite large enough a fraction of molecules.

Rhenium-thyrosine: If a large enough fraction of this complex can be excited, the x-ray changes that would accompany the reaction would be easy to follow for rather small concentrations of complex. The requirements for obtaining a high enough fraction excited are not yet known.

Osmium-ruthenium: By creating complexes of this kind with tailor-made bridging ligands, it is likely that time scales long enough for initial time-resolved studies can be obtained. Monitoring both the donator atom and the acceptor atom ought to give useful information about the electron movement. Unfortunately, a few of the Os and Ru band edges are quite close to each other. Since both band edges will change after excitation, it will be difficult to determine what changes are related to which atom.

10.4 High-energy advantages

Working at high energies (say, above 8 keV) avoids essentially all problems that would hamper investigations at lower energies (less than, say, 4 keV):

- The experiment does not have to be carried out in a vacuum or helium atmosphere.
- Absorption by the solvent will not be a problem, as long as the solvent used does not contain any heavy elements (such as chlorine). This makes it possible to use longer, more practical path lengths.
- No special materials such as Kapton have to be used for sample-cell walls. This greatly simplifies the construction of the cells and offers new opportunities, such as introducing electrochemical equipment into the cell so that the reaction can be induced *in situ* without a laser.

The smaller number of photons available at 10 keV somewhat offsets these advantages, but with fewer photons lost in the experimental setup, it may very well yield better results.

11 Acknowledgements

I would like to thank my supervisor Professor Jörgen Larsson and Professor Villy Sundström for offering me the opportunity to do this master's thesis, and for assistance and support provided during the course of the project.

I would like to thank doctor Robert Smith, with whom this project was carried out in close cooperation, for all the assistance, encouragement and advice he gave me during this work.

I would like to thank doctor Hartwig Modrow for the experimental results from ELSA in Bonn.

I would like to thank the researchers working at the beamline, Tue Hansen, Michael Harbst, Peter Sondhauss and Ola Synnergren, for providing company and a lot of support when experiments were carried out at D611.

12 Bibliography

References

[1] R Prins, D. C. Koningsberger et al, *X-Ray Absorption: Principles, Applications, Techniques of EXAFS, SEXAFS and XANES*

[2] George Meitzner, *Experimental aspects of X-Ray absorption spectroscopy*, Catalysis Today **39** 281-291 (1998)

[3] Jun Kawai, *Absorption Techniques in X-ray Spectrometry*, Encyclopedia of Analytical Chemistry, 13288-13315

[4] Matthew Newville, *Fundamentals of XAFS*, Consortium for Advanced Radiation Sources, University of Chicago

[5] W. R. Leo, *Techniques for Nuclear and Particle Physics Experiments*

[6] *X-Ray Form Factor, Attenuation, and Scattering Tables*, http://physics.nist.gov/ PhysRefData/FFast/html/form.html

[7] *The XAFS Model Compound Library*, http://cars9.uchicago.edu/ newville/ModelLib/

[8] Richard Neutze, Remco Wouts, Simone Techert, jan Davidsson, Menhard Kocsis, Adam Kirrander, Friedrich Schotte, Michael Wulff, *Visualizing Photochemical Dynamics in Solution through Picosecond X-Ray Scattering*, Phys. Rev. Lett. **87** 195508 (2001)

[9] Alexander N. Tarnovsky, Jose-Luis Alvarez, Arkady P. Yartsev, Villy Sundström, Eva Åkesson, *Photodissociation dynamics of diiodomethane in solution*, Chem. Phys. Lett, **312** 121 (1999)

[10] Alexander N. Tarnovsky, Villy Sundström, Eva Åkesson, Torbjörn Pascher, *Photochemistry of Diiodomethane in Solution Studied by Femtosecond and Nanosecond Laser Photolysis. Formation and Dark Reactions of the CH_2-I Isomer Photoproduct and its Role in Cyclopropanation of Olefins*

[11] Christian Bressler, Melanie Saes, Majed Chergui, Philip Pattison, Daniel Grolimund, Rafael Abela, *Towards structural dynamics in condensed chemical systems exploiting ultrafast time-resolved x-ray absorption spectroscopy*, J. Chem. Phys, **116** 2955 (2002)

[12] Charles Kittel, *Introduction to Solid State Physics*

[13] Brian O'Regan, Michael Grätzel, *A low-cost, high-efficiency solar cell based on dye-sensitized colloidal TiO_2 films*, Nature, **353**, 737 (1991)

[14] Balzani, V.; Juris, A.; Venturi, M.; Campagna, S.; Serroni, S., *Luminescent and Redox-Active Polynuclear Transition Metal Complexes*, Chem. Rev. **96** 759-834 (1996)

[15] M.K. Nazeeruddin et al, *Conversion of Light to Electricity by* cis-X_2*Bis(2,2'-bipyridil-4,4'-dicarboxylate)ruthenium(II) Charge-Transfer Sensitizers (X = Cl^-, Br^-, I^-, CN^-, and SCN^-) on Nanocrystalline TiO_2 Electrodes*, J. Am. Chem. Soc, **115** 6382 (1993)

[16] Villy Sundström et al, *Electron Transfer from the Singlet and Triplet Excited States of* $Ru(dcbpy)_3(NCS)_2$ *into Nanocrystalline* TiO_2 *Thin Films*, J. Phys. Chem. B, **106** 4396-4404 (2002)

[17] *Efficient panchromatic sensitization of nanocrystalline* TiO2 *films by a black dye based on a trithiocyanato-ruthenium complex*, Chemical Communications **18** 1705 (1997)

[18] Raed Granem, Yunhua Xu, Jie Pan, Tobias Hoffmann, Johan Andersson, Tomáš Polívka, Torbjörn Pascher, Stenbjörn Styring, Licheng Sun, Villy Sundström, *Light-Driven Tyrosine Radical Formation in Ruthenium-Tyrosine Complex Attached to Nanoparticle TiO_2*, Inorg Chem, **41**, 6258-6266 (2002)

[19] *Near-Infrared Luminiescence of Supramolecular Species Consisting of Osmium(II)- and/or Ruthenium(II)-Polypyridine Components*, Inorg. Chem. **33** 1491-1496 (1994)

[20] Giorgio Margaritondo, *Introduction to Synchrotron Radiation*, Oxford University Press, 1988

[21] *X-Ray data booklet*, Center for x-ray Optics and Advanced Light Source, Lawrence Berkeley National Laboratory. See http://xdb.lbl.gov/

[22] Jörgen Larsson, *Laser and Synchrotron Radiation Pump-Probe X-Ray Diffraction Experiments*, Meas. Sci. Technol. **12** 1835 (2001)

[23] *XANES of Cl-naphtalene in* CH_3I *solvent*, ChemPhys **289** 281 (2003)

[24] T. K. Sham, *X-ray absorption spectra of ruthenium L edges in hexaammineruthenium trichloride*, J. Am. Chem. Soc. **105** 2269 (1983)

[25] Alfred Q. R. Baron, *Avalanche Photodiodes (APDs) as Fast X-Ray Detectors*

[26] Henke B L., Knauer J-P and Premaratne K, *The characterization of x-ray photocathodes in the 0.1-10-keV photon energy region*, J. Appl. Phys. **52** 1509 (1981)

[27] *Atomic Scattering Factors*, http://www-cxro.lbl.gov/optical_constants/

[28] Melaine Saes, Christian Bressler, Rafael Abela, Daniel Grolimund, Steven L. Johnsson, Philip A. Heimann, Majed Chergui, *Observing Photochemical Transients by Ultrafast X-Ray Absorption Spectroscopy*, Phys. Rev. Lett. **90** 047403 (2003)

A Band edge tables

Element		K	L_I	L_{II}	L_{III}	M_I	M_{II}	M_{III}	M_{IV}	M_V
1	H									
2	He									
3	Li	55	5							
4	Be	111	8							
5	B	188	13	5						
6	C	284	20	6						
7	N	402	26	9	9					
8	O	532	24	7	7					
9	F	685	31	9	9					
10	Ne	867	45	18	18					
11	Na	1072	63	31	31					
12	Mg	1305	89	51	51					
13	Al	1560	118	73	73	8				
14	Si	1839	149	99	99	11	5			
15	P	2146	189	132	132	14	6	6		
16	S	2472	229	165	165	18	8	8		
17	Cl	2822	270	202	200	18	7	7		
18	Ar	3203	320	247	245	25	12	12		
19	K	3607	377	296	294	34	18	18		
20	Ca	4038	438	350	346	44	25	25		
21	Sc	4493	500	407	402	54	32	32		
22	Ti	4966	564	462	456	60	35	35		
23	V	5465	628	520	513	66	38	38	2	
24	Cr	5989	695	584	574	74	42	42	2	2
25	Mn	6539	769	651	640	84	49	49	7	7
26	Fe	7112	846	721	708	93	54	54	4	4
27	Co	7709	926	794	779	101	60	60	3	3
28	Ni	8333	1008	872	855	112	68	68	4	4
29	Cu	8979	1096	951	931	120	74	74	2	2
30	Zn	9659	1194	1043	1020	136	87	87	8	8
31	Ga	10367	1298	1142	1115	158	107	103	17	17
32	Ge	11103	1414	1248	1217	180	128	121	29	29
33	As	11867	1526	1359	1323	204	146	140	41	41
34	Se	12658	1654	1476	1436	232	168	162	57	57
35	Br	13474	1782	1596	1550	256	189	182	70	69
36	Kr	14326	1921	1727	1675	288	223	214	89	89
37	Rb	15200	2065	1864	1804	322	247	238	112	110
38	Sr	16105	2216	2007	1940	358	280	269	135	133
39	Y	17038	2372	2156	2080	394	312	300	160	157
40	Zr	17998	2532	2307	2222	430	344	330	182	180
41	Nb	18986	2698	2465	2370	468	378	363	207	205
42	Mo	20000	2866	2625	2520	505	410	392	230	227
43	Tc	21044	3042	2793	2677	548	445	425	256	253
44	Ru	22117	3224	2967	2838	585	483	461	284	279
45	Rh	23220	3412	3146	3004	627	521	496	312	307
46	Pd	24350	3604	3330	3173	670	559	532	340	335
47	Ag	25514	3806	3524	3351	718	602	571	373	367
48	Cd	26711	4018	3727	3538	770	651	616	410	404
49	In	27940	4238	3938	3730	826	702	664	451	443
50	Sn	29200	4465	4156	3929	884	756	714	493	485

Table 2: The x-ray band-edge energies (in eV) for the K-, L- and M-edges of elements 1–50. Data from [6].

Element		K	L_I	L_{II}	L_{III}	M_I	M_{II}	M_{III}	M_{IV}	M_V
51	Sb	30491	4698	4380	4132	944	812	766	537	528
52	Te	31814	4939	4612	4341	1006	870	819	582	572
53	I	33169	5188	4852	4557	1072	930	875	631	619
54	Xe	34561	5453	5104	4782	1145	999	937	685	672
55	Cs	35985	5714	5359	5012	1217	1065	998	740	726
56	Ba	37441	5989	5624	5247	1293	1137	1062	796	781
57	La	38925	6266	5891	5483	1361	1204	1123	848	832
58	Ce	40443	6549	6164	5723	1435	1273	1185	901	883
59	Pr	41991	6835	6440	5964	1511	1337	1242	951	931
60	Nd	43569	7126	6722	6208	1575	1403	1297	1000	978
61	Pm	45184	7428	7013	6459	1646	1471	1357	1052	1027
62	Sm	46834	7737	7312	6716	1723	1541	1420	1106	1080
63	Eu	48519	8052	7617	6977	1800	1614	1481	1161	1131
64	Gd	50239	8376	7930	7243	1881	1688	1544	1217	1185
65	Tb	51996	8708	8252	7514	1968	1768	1611	1275	1241
66	Dy	53788	9046	8581	7790	2047	1842	1676	1332	1295
67	Ho	55618	9394	8918	8071	2128	1923	1741	1392	1351
68	Er	57486	9751	9264	8358	2206	2006	1812	1453	1409
69	Tm	59390	10116	9617	8648	2307	2090	1884	1515	1468
70	Yb	61332	10486	9978	8944	2398	2173	1950	1576	1528
71	Lu	63314	10870	10349	9244	2491	2264	2024	1639	1588
72	Hf	65351	11271	10739	9561	2601	2365	2108	1716	1662
73	Ta	67416	11682	11136	9881	2708	2469	2194	1793	1735
74	W	69525	12100	11544	10207	2820	2575	2281	1872	1809
75	Re	71676	12527	11959	10535	2932	2682	2367	1949	1883
76	Os	73871	12968	12385	10871	3048	2792	2457	2031	1960
77	Ir	76111	13418	12824	11215	3174	2909	2551	2116	2040
78	Pt	78395	13880	13273	11564	3296	3026	2645	2202	2122
79	Au	80725	14353	13734	11919	3425	3148	2743	2291	2206
80	Hg	83102	14839	14209	12284	3562	3278	2847	2385	2295
81	Tl	85530	15347	14698	12658	3704	3416	2957	2485	2389
82	Pb	88004	15861	15200	13035	3851	3554	3066	2586	2484
83	Bi	90526	16388	15711	13419	3999	3696	3177	2688	2580
84	Po	93105	16939	16244	13814	4149	3854	3302	2798	2683
85	At	95730	17493	16785	14214	4317	4008	3426	2909	2787
86	Rn	98404	18049	17337	14619	4482	4159	3538	3022	2892
87	Fr	101137	18639	17906	15031	4652	4327	3663	3136	3000
88	Ra	103922	19237	18484	15444	4822	4490	3792	3248	3105
89	Ac	106755	19840	19083	15871	5002	4656	3909	3370	3219
90	Th	109651	20472	19693	16300	5182	4830	4046	3491	3332
91	Pa	112601	21105	20314	16733	5367	5001	4174	3611	3442
92	U	115606	21757	20948	17166	5548	5182	4303	3728	3552

Table 3: The x-ray band-edge energies (in eV) for the K-, L- and M-edges of elements 51–92. Data from [6].

1006	Te M_I	1540.7	Sm M_{II}	2201.9	Pt M_{IV}	2966.9	Ru L_{II}
1008.1	Ni L_I	1544	Gd M_{III}	2205.7	Au M_V	2999.7	Fr M_V
1019.7	Zn L_{III}	1549.9	Br L_{III}	2206.5	Er M_I	3003.8	Rh L_{III}
1026.9	Pm M_V	1559.6	Al K	2216.3	Sr L_I	3021.5	Rn M_{IV}
1042.8	Zn L_{II}	1575.3	Nd M_I	2222.3	Zr L_{III}	3026.5	Pt M_{II}
1051.5	Pm M_{IV}	1576.3	Yb M_{IV}	2263.5	Lu M_{II}	3042.5	Tc L_I
1062.2	Ba M_{III}	1588.5	Lu M_V	2281	W M_{III}	3048.5	Os M_I
1065	Cs M_{II}	1596	Br L_{II}	2291.1	Au M_{IV}	3066.4	Pb M_{III}
1072.1	I M_I	1611.3	Tb M_{III}	2294.9	Hg M_V	3104.9	Ra M_V
1072.1	Na K	1613.9	Eu M_{II}	2306.7	Zr L_{II}	3136.2	Fr M_{IV}
1080.2	Sm M_V	1639.4	Lu M_{IV}	2306.8	Tm M_I	3146.1	Rh L_{II}
1096.1	Cu L_I	1646.5	Pm M_I	2365.4	Hf M_{II}	3147.8	Au M_{II}
1106	Sm M_{IV}	1653.9	Se L_I	2367.3	Re M_{III}	3173.3	Pd L_{III}
1115.4	Ga L_{III}	1661.7	Hf M_V	2370.5	Nb L_{III}	3173.7	Ir M_I
1123.4	La M_{III}	1674.9	Kr L_{III}	2372.5	Y L_I	3176.9	Bi M_{III}
1130.9	Eu M_V	1675.6	Dy M_{III}	2384.9	Hg M_{IV}	3202.9	Ar K
1136.7	Ba M_{II}	1688.3	Gd M_{II}	2389.3	Tl M_V	3219	Ac M_V
1142.3	Ga L_{II}	1716.4	Hf M_{IV}	2398.1	Yb M_I	3224	Ru L_I
1144.6	Xe M_I	1722.8	Sm M_I	2457.2	Os M_{III}	3248.4	Ra M_{IV}
1160.6	Eu M_{IV}	1727.2	Kr L_{II}	2464.7	Nb L_{II}	3278.5	Hg M_{II}
1185.2	Gd M_V	1735.1	Ta M_V	2468.7	Ta M_{II}	3296	Pt M_I
1185.4	Ce M_{III}	1741.2	Ho M_{III}	2472	S K	3301.9	Po M_{III}
1193.6	Zn L_I	1767.7	Tb M_{II}	2484	Pb M_V	3330.3	Pd L_{II}
1204.4	La M_{II}	1782	Br L_I	2485.1	Tl M_{IV}	3332	Th M_V
1216.7	Ge L_{III}	1793.2	Ta M_{IV}	2491.2	Lu M_I	3351.1	Ag L_{III}
1217.1	Cs M_I	1800	Eu M_I	2520.2	Mo L_{III}	3370.2	Ac M_{IV}
1217.2	Gd M_{IV}	1804.4	Rb L_{III}	2531.6	Zr L_I	3411.9	Rh L_I
1241.2	Tb M_V	1809.2	W M_V	2550.7	Ir M_{III}	3415.7	Tl M_{II}
1242.2	Pr M_{III}	1811.8	Er M_{III}	2574.9	W M_{II}	3424.9	Au M_I
1247.8	Ge L_{II}	1838.9	Si K	2579.6	Bi M_V	3426	At M_{III}
1272.8	Ce M_{II}	1841.8	Dy M_{II}	2585.6	Pb M_{IV}	3441.8	Pa M_V
1275	Tb M_{IV}	1863.9	Rb L_{II}	2600.9	Hf M_I	3490.8	Th M_{IV}
1292.8	Ba M_I	1871.6	W M_{IV}	2625.1	Mo L_{II}	3523.7	Ag L_{II}
1294.9	Dy M_V	1880.8	Gd M_I	2645.4	Pt M_{III}	3537.5	Cd L_{III}
1297.4	Nd M_{III}	1882.9	Re M_V	2676.9	Tc L_{III}	3538	Rn M_{III}
1297.7	Ga L_I	1884.5	Tm M_{III}	2681.6	Re M_{II}	3551.7	U M_V
1305	Mg K	1921	Kr L_I	2683	Po M_V	3554.2	Pb M_{II}
1323.1	As L_{III}	1922.8	Ho M_{II}	2687.6	Bi M_{IV}	3561.6	Hg M_I
1332.5	Dy M_{IV}	1939.6	Sr L_{III}	2697.7	Nb L_I	3604.3	Pd L_I
1337.4	Pr M_{II}	1948.9	Re M_{IV}	2708	Ta M_I	3607.4	K K
1351.4	Ho M_V	1949.8	Yb M_{III}	2743	Au M_{III}	3611.2	Pa M_{IV}
1356.9	Pm M_{III}	1960.1	Os M_V	2786.7	At M_V	3663	Fr M_{III}
1358.6	As L_{II}	1967.5	Tb M_I	2792.2	Os M_{II}	3696.3	Bi M_{II}
1361.3	La M_I	2005.8	Er M_{II}	2793.2	Tc L_{II}	3704.1	Tl M_I
1391.5	Ho M_{IV}	2006.8	Sr L_{II}	2798	Po M_{IV}	3727	Cd L_{II}
1402.8	Nd M_{II}	2023.6	Lu M_{III}	2819.6	W M_I	3727.6	U M_{IV}
1409.3	Er M_V	2030.8	Os M_{IV}	2822.4	Cl K	3730.1	In L_{III}
1414.3	Ge L_I	2040.4	Ir M_V	2837.9	Ru L_{III}	3791.8	Ra M_{III}
1419.8	Sm M_{III}	2046.8	Dy M_I	2847.1	Hg M_{III}	3805.8	Ag L_I
1434.6	Ce M_I	2065.1	Rb L_I	2865.5	Mo L_I	3850.7	Pb M_I
1435.8	Se L_{III}	2080	Y L_{III}	2892.4	Rn M_V	3854.1	Po M_{II}
1453.3	Er M_{IV}	2089.8	Tm M_{II}	2908.7	At M_{IV}	3909	Ac M_{III}
1467.7	Tm M_V	2107.6	Hf M_{III}	2908.7	Ir M_{II}	3928.8	Sn L_{III}
1471.4	Pm M_{II}	2116.1	Ir M_{IV}	2931.7	Re M_I	3938	In L_{II}
1476.2	Se L_{II}	2121.6	Pt M_V	2956.6	Tl M_{III}	3999.1	Bi M_I
1480.6	Eu M_{III}	2128.3	Ho M_I				
1511	Pr M_I	2145.5	P K				
1514.6	Tm M_{IV}	2155.5	Y L_{II}				
1526.5	As L_I	2173	Yb M_{II}				
1527.8	Yb M_V	2194	Ta M_{III}				

Table 4: Band-edges sorted by energy, for band edges above 1 keV. Only the K-, L- and M-edges are included. For band edges above 4 keV, see the table on next page. Data from [6].

4008	At M_{II}	6834.8	Pr L_I	12657.8	Se K	29200.1	Sn K
4018	Cd L_I	6976.9	Eu L_{III}	12824.1	Ir L_{II}	30491.2	Sb K
4038.1	Ca K	7012.8	Pm L_{II}	12968	Os L_I	31813.8	Te K
4046.1	Th M_{III}	7112	Fe K	13035.2	Pb L_{III}	33169.4	I K
4132.2	Sb L_{III}	7126	Nd L_I	13272.6	Pt L_{II}	34561.4	Xe K
4149.4	Po M_I	7242.8	Gd L_{III}	13418.5	Ir L_I	35984.6	Cs K
4156.1	Sn L_{II}	7311.8	Sm L_{II}	13418.6	Bi L_{III}	37440.6	Ba K
4159	Rn M_{II}	7427.9	Pm L_I	13473.7	Br K	38924.6	La K
4173.8	Pa M_{III}	7514	Tb L_{III}	13733.6	Au L_{II}	40443	Ce K
4237.5	In L_I	7617.1	Eu L_{II}	13813.8	Po L_{III}	41990.6	Pr K
4303.4	U M_{III}	7708.9	Co K	13879.9	Pt L_I	43568.9	Nd K
4317	At M_I	7736.8	Sm L_I	14208.7	Hg L_{II}	45184	Pm K
4327	Fr M_{II}	7790.1	Dy L_{III}	14213.5	At L_{III}	46834.2	Sm K
4341.4	Te L_{III}	7930.3	Gd L_{II}	14325.6	Kr K	48519	Eu K
4380.4	Sb L_{II}	8052	Eu L_I	14352.8	Au L_I	50239.1	Gd K
4464.7	Sn L_I	8071.1	Ho L_{III}	14619.4	Rn L_{III}	51995.7	Tb K
4482	Rn M_I	8251.6	Tb L_{II}	14697.9	Tl L_{II}	53788.5	Dy K
4489.5	Ra M_{II}	8332.8	Ni K	14839.3	Hg L_I	55617.7	Ho K
4492.8	Sc K	8357.9	Er L_{III}	15031.2	Fr L_{III}	57485.5	Er K
4557.1	I L_{III}	8375.6	Gd L_I	15199.7	Rb K	59389.6	Tm K
4612	Te L_{II}	8580.6	Dy L_{II}	15200	Pb L_{II}	61332.3	Yb K
4652	Fr M_I	8648	Tm L_{III}	15346.7	Tl L_I	63313.8	Lu K
4656	Ac M_{II}	8708	Tb L_I	15444.4	Ra L_{III}	65350.8	Hf K
4698.3	Sb L_I	8917.8	Ho L_{II}	15711.1	Bi L_{II}	67416.4	Ta K
4782.2	Xe L_{III}	8943.6	Yb L_{III}	15860.8	Pb L_I	69525	W K
4822	Ra M_I	8978.9	Cu K	15871	Ac L_{III}	71676.4	Re K
4830.4	Th M_{II}	9045.8	Dy L_I	16104.6	Sr K	73870.8	Os K
4852.1	I L_{II}	9244.1	Lu L_{III}	16244.3	Po L_{II}	76111	Ir K
4939.2	Te L_I	9264.3	Er L_{II}	16300.3	Th L_{III}	78394.8	Pt K
4966.4	Ti K	9394.2	Ho L_I	16387.5	Bi L_I	80724.9	Au K
5000.9	Pa M_{II}	9560.7	Hf L_{III}	16733.1	Pa L_{III}	83102.3	Hg K
5002	Ac M_I	9616.9	Tm L_{II}	16784.7	At L_{II}	85530.4	Tl K
5011.9	Cs L_{III}	9658.6	Zn K	16939.3	Po L_I	88004.5	Pb K
5103.7	Xe L_{II}	9751.3	Er L_I	17038.4	Y K	90525.9	Bi K
5182.2	U M_{II}	9881.1	Ta L_{III}	17166.3	U L_{III}	93105	Po K
5182.3	Th M_I	9978.2	Yb L_{II}	17337.1	Rn L_{II}	95729.9	At K
5188.1	I L_I	10115.7	Tm L_I	17493	At L_I	98404	Rn K
5247	Ba L_{III}	10206.8	W L_{III}	17906.5	Fr L_{II}	101137	Fr K
5359.4	Cs L_{II}	10348.6	Lu L_{II}	17997.6	Zr K	103922	Ra K
5366.9	Pa M_I	10367.1	Ga K	18049	Rn L_I	106755	Ac K
5452.8	Xe L_I	10486.4	Yb L_I	18484.3	Ra L_{II}	109651	Th K
5465.1	V K	10535.3	Re L_{III}	18639	Fr L_I	112601	Pa K
5482.7	La L_{III}	10739.4	Hf L_{II}	18985.6	Nb K	115606	U K
5548	U M_I	10870.4	Lu L_I	19083.2	Ac L_{II}		
5623.6	Ba L_{II}	10870.9	Os L_{III}	19236.7	Ra L_I		
5714.3	Cs L_I	11103.1	Ge K	19693.2	Th L_{II}		
5723.4	Ce L_{III}	11136.1	Ta L_{II}	19840	Ac L_I		
5890.6	La L_{II}	11215.2	Ir L_{III}	19999.5	Mo K		
5964.3	Pr L_{III}	11270.7	Hf L_I	20313.7	Pa L_{II}		
5988.8	Ba L_I	11544	W L_{II}	20472.1	Th L_I		
5989.2	Cr K	11563.7	Pt L_{III}	20947.6	U L_{II}		
6164.2	Ce L_{II}	11681.5	Ta L_I	21044	Tc K		
6207.9	Nd L_{III}	11866.7	As K	21104.6	Pa L_I		
6266.3	La L_I	11918.7	Au L_{III}	21757.4	U L_I		
6440.4	Pr L_{II}	11958.7	Re L_{II}	22117.2	Ru K		
6459.3	Pm L_{III}	12099.8	W L_I	23219.9	Rh K		
6539	Mn K	12283.9	Hg L_{III}	24350.3	Pd K		
6548.8	Ce L_I	12385	Os L_{II}	25514	Ag K		
6716.2	Sm L_{III}	12526.7	Re L_I	26711.2	Cd K		
6721.5	Nd L_{II}	12657.5	Tl L_{III}	27939.9	In K		

Table 5: Band-edges sorted by energy. Only the K-, L- and M-edges are included. For energies below 4 keV, see the table on the previous page. Data from [6].